Modelling the supernova-driven ISM in different environments

A. Gatto,[1]★ S. Walch,[1,2] M.-M. Mac Low,[3] T. Naab,[1] P. Girichidis,[1] S. C. O. Glover,[4]
R. Wünsch,[5] R. S. Klessen,[4,6,7] P. C. Clark,[4,8] C. Baczynski,[3,4] T. Peters,[1,9]
J. P. Ostriker,[10,11] J. C. Ibáñez-Mejía[3,4] and S. Haid[2]

[1]*Max-Planck-Institut für Astrophysik, Karl-Schwarzschild-Strasse 1, D-85748 Garching, Germany*
[2]*Physikalisches Institut, Universität Köln, Zülpicher Strasse 77, D-50937 Köln, Germany*
[3]*Department of Astrophysics, American Museum of Natural History, 79th Street at Central Park West, New York, NY 10024, USA*
[4]*Institut für Theoretische Astrophysik, Zentrum für Astronomie, Universität Heidelberg, Albert-Ueberle-Str. 2, D-69120 Heidelberg, Germany*
[5]*Astronomický Ústav, Akademie věd České Republiky, Boční II 1401, CZ-14131 Praha, Czech Republic*
[6]*Department of Astronomy and Astrophysics, University of California, 1156 High Street, Santa Cruz, CA 95064, USA*
[7]*Kavli Institute for Particle Astrophysics and Cosmology, Stanford University, SLAC Nat. Acc. Lab., Menlo Park, CA 94025, USA*
[8]*School of Physics and Astronomy, Cardiff University, 5 The Parade, Cardiff CF24 3AA, UK*
[9]*Institut für Computergestützte Wissenschaften, Universität Zürich, Winterthurerstrasse 190, CH-8057 Zürich, Switzerland*
[10]*Department of Astrophysical Sciences, Princeton University, 4 Ivy Ln, Princeton, NJ 08544, USA*
[11]*Department of Astronomy, Columbia University, 550 West 120th Street, New York, NY 10027, USA*

ABSTRACT

We use hydrodynamical simulations in a $(256\,\mathrm{pc})^3$ periodic box to model the impact of
supernova (SN) explosions on the multiphase interstellar medium (ISM) for initial densities
$n = 0.5$–30 cm^{-3} and SN rates 1–720 Myr^{-1}. We include radiative cooling, diffuse heating,
and the formation of molecular gas using a chemical network. The SNe explode either at
random positions, at density peaks, or both. We further present a model combining thermal
energy for resolved and momentum input for unresolved SNe. Random driving at high SN
rates results in hot gas ($T \gtrsim 10^6$ K) filling >90 per cent of the volume. This gas reaches high
pressures ($10^4 < P/k_\mathrm{B} < 10^7$ K cm^{-3}) due to the combination of SN explosions in the hot,
low-density medium and confinement in the periodic box. These pressures move the gas from
a two-phase equilibrium to the single-phase, cold branch of the cooling curve. The molecular
hydrogen dominates the mass (>50 per cent), residing in small, dense clumps. Such a model
might resemble the dense ISM in high-redshift galaxies. Peak driving results in huge radiative
losses, producing a filamentary ISM with virtually no hot gas, and a small molecular hydrogen
mass fraction (≪1 per cent). Varying the ratio of peak to random SNe yields ISM properties
in between the two extremes, with a sharp transition for equal contributions. The velocity
dispersion in H I remains $\lesssim 10$ km s^{-1} in all cases. For peak driving, the velocity dispersion in
Hα can be as high as 70 km s^{-1} due to the contribution from young, embedded SN remnants.

Key words: methods: numerical – ISM: evolution – ISM: kinematics and dynamics – ISM:
structure – ISM: supernova remnants – galaxies: evolution.

1 INTRODUCTION

Supernova (SN) explosions are an important component for shaping
the interstellar medium (ISM). In particular, they produce its hottest
phase, with temperature $T \gtrsim 10^6$ K (Cox & Smith 1974; McKee &
Ostriker 1977). In the Milky Way, this hot phase fills from 20 to
80 per cent of the volume with increasing height above the disc
(Ferrière 2001; Kalberla & Dedes 2008). SNe also drive turbulent

motions in the ISM gas (Norman & Ferrara 1996; Joung & Mac
Low 2006; de Avillez & Breitschwerdt 2007; Gent et al. 2013),
although their relative importance with respect to other driving
mechanisms has yet to be fully determined (see e.g. Mestel &
Spitzer 1956; Sellwood & Balbus 1999; Kritsuk & Norman 2002;
Wada, Meurer & Norman 2002; Tamburro et al. 2009; Klessen &
Hennebelle 2010).

Supersonic turbulent motions in warm and cold gas, observed in
emission from H I, have been found in many local and extragalactic
environments, with a typical one-dimensional velocity dispersion of
$\sigma \simeq 10$ km s^{-1} (e.g. Heiles & Troland 2003; Petric & Rupen 2007;

Tamburro et al. 2009). Similar velocity dispersions for molecular gas have been found from CO emission lines at galactic scales (Caldú-Primo et al. 2013), with a decrease to a few kilometres per second when observing small, isolated molecular structures (Larson 1981) and a transition to transonic motions at the scale of dense cores (∼0.1 pc; Goodman et al. 1998). Globally, these random motions could provide an effective turbulent pressure (Ostriker, McKee & Leroy 2010) and help to regulate star formation (Elmegreen & Scalo 2004; Mac Low & Klessen 2004).

SNe are able to heat up the ISM, influencing its pressure and dispersing the gas locally (e.g. McKee & Ostriker 1977; de Avillez & Breitschwerdt 2004, 2007; Mac Low et al. 2005; Joung & Mac Low 2006; Joung, Mac Low & Bryan 2009). However, they could also sweep up the medium, causing colliding flows that may trigger new molecular cloud and star formation events (Elmegreen & Lada 1977; Heitsch et al. 2006; Vázquez-Semadeni et al. 2006; Banerjee et al. 2009; Heitsch, Naab & Walch 2011).

Type II SN progenitors are massive OB stars with typically low space velocities of ≈ 15 km s^{-1} (Stone 1991). Due to these velocities, they can only travel tens to hundreds of parsecs away from their birthplaces during their lifetimes. However, 10–30 per cent of O stars and 5–10 per cent of B stars in the Galaxy are runaway stars, which have large velocities (from 30 to a few hundred km s^{-1}; Blaauw 1961; Gies & Bolton 1986; Gies 1987; Stone 1991) and are therefore found far from associations (from several hundred parsecs to a kiloparsec away from their birthplaces). Runaway stars are produced by dynamical ejection by means of gravitational scattering (Gies & Bolton 1986; Fujii & Portegies Zwart 2011; Perets & Šubr 2012), by massive binary systems where one of the two stars explodes as an SN, which leads to the ejection of the unbound companion (Blaauw 1961; Portegies Zwart 2000; Eldridge, Langer & Tout 2011), or both mechanisms (Pflamm-Altenburg & Kroupa 2010).

Runaway massive stars typically explode in the diffuse ISM, i.e. in random positions, which are not correlated with the dense molecular clouds within which massive star formation takes place. This also applies to Type Ia SNe, which add an additional random component of SN explosions due to the long lifetimes of their progenitors.

A high fraction of massive stars (70–90 per cent; Lada & Lada 2003) also form in clusters and associations, rather than in isolation. Despite being initially embedded in high-density environments, the high degree of clustering and multiplicity of Type II SN progenitors causes the majority of SN explosions to happen within low-density gas that has previously been processed by the combined effect of stellar winds (Tenorio-Tagle et al. 1990, 1991; Brighenti & D'Ercole 1994; Rogers & Pittard 2013) and H II regions (Gritschneder et al. 2009; Walch et al. 2012, 2013; Dale et al. 2014), as well as earlier SNe in superbubbles (McCray & Kafatos 1987; Mac Low & McCray 1988; Tenorio-Tagle & Bodenheimer 1988). However, there is evidence that SNe are also interacting with the dense gas. In the inner Galaxy, around 15 per cent of identified SN remnants show clear signs of interaction with molecular gas, including water maser emission (Hewitt & Yusef-Zadeh 2009) and TeV γ-ray emission (Fukui et al. 2003). Overall, SNe that explode in any of the above low-density environments can be approximated by explosions at random positions in an ISM with a significant volume filling fraction (VFF) of hot gas. The remaining fraction of SNe interacting with dense gas can be modelled via explosions within the densest gas parcels (Walch & Naab 2014).

Several studies of the SN-driven ISM have been carried out in the past, assuming clustered, random or density peak positions for the explosions. For instance, de Avillez & Breitschwerdt (2004) studied a representative piece of a stratified galactic disc, shaped by SNe going off at fixed rate and mostly placed in regions with highest density. Joung & Mac Low (2006) performed similar simulations but chose random positions for their explosion locations. In a recent paper, Hennebelle & Iffrig (2014) perform magnetohydrodynamical simulations of a stratified Galactic disc modelling star formation via star cluster sink particles. They show that SN explosions correlated in space and time with the particles' position and accretion can significantly inhibit further star formation. Similar conclusions have been drawn in Iffrig & Hennebelle (2014). A massive star exploding outside of the dense gas has a limited effect with respect to the case where the explosion is located within the cloud. In the latter case, a higher fraction of momentum is transferred to the cold gas and up to half of the cloud's mass can be removed by the SN. Despite the number of previous works investigating the effect of SNe on both stratified (e.g. Hill et al. 2012; Shetty & Ostriker 2012; Gent et al. 2013; Kim, Ostriker & Kim 2013a) and unstratified ISM (see e.g. Balsara et al. 2004; Kim 2004; Mac Low et al. 2005; Slyz et al. 2005; Dib, Bell & Burkert 2006, for modelling in periodic boxes), a systematic study is missing of the impact of different assumed SN positions, as well as the consequences of varying the SN rate with the gas density.

In this paper, we model the turbulent, multiphase ISM in regions of different mean density over a time-scale of ∼100 Myr with fixed (Type II) SN rates, which are informed by the Kennicutt–Schmidt (KS) relation (Schmidt 1959; Kennicutt 1998). We include a chemical network allowing us to partially model the effects of non-equilibrium chemistry in the warm gas, as well as the formation of H$_2$ and CO including dust and self-shielding. We focus on three different scientific questions:

(i) Given a certain initial gas density, how do the properties of the ISM depend on the assumed SN rate?
(ii) What are the differences between a medium shaped by SNe placed randomly or at density peaks?
(iii) How does the ISM change as a function of the ratio between SNe that explode randomly or at density peaks?

The paper is organized as follows: in Section 2, we describe our model and runs. In Section 3, we show our results. Finally, we present our conclusions in Section 4.

2 NUMERICAL METHOD, PARAMETERS, AND RUNS

2.1 Simulation method

We use the Eulerian, adaptive mesh refinement, hydrodynamic code FLASH 4 (Fryxell et al. 2000; Dubey et al. 2008; Dubey et al. 2013) to model the SN-driven ISM in three-dimensional (3D) simulations. We use the directionally split, Bouchut HLL5R solver (Bouchut, Klingenberg & Waagan 2007; Waagan 2009; Bouchut, Klingenberg & Waagan 2010) to simulate a volume of (256 pc)^3 with periodic boundary conditions. For the majority of the simulations, the resolution is fixed to 128^3 cells ($\Delta x = 2$ pc), but we run a few setups at higher resolution (see Section 3.8). In different simulations, we change the initial total number density of the box from $n_i = 0.5$ cm^{-3} to $n_i = 30$ cm^{-3} (see Table 1) and the initial temperature is 6000 K.

Table 1. Parameters of the simulations. Column 1 gives the mean volume density n_i and column 2 gives the corresponding gas surface density. In column 3–5, we list the simulated SN rates, where $\dot{N}_{\rm SN,KS}$ is derived from equation (2).

n_i (cm^{-3})	$\Sigma_{\rm gas}$ (M$_\odot$ pc^{-2})	$\dot{N}_{\rm SN,-}$ (Myr^{-1})	$\dot{N}_{\rm SN,KS}$ (Myr^{-1})	$\dot{N}_{\rm SN,+}$ (Myr^{-1})
0.5	4.1	–	1.2	–
1	8.1	1.5	3	6
3	24.3	7	14	28
10	81.2	38.5	77	154
30	243	180	360	720

2.2 Gas cooling and chemistry

We include a chemical network to treat radiative cooling and diffuse heating as well as molecule formation. In the cold and warm gas, the main contributions to the cooling rate come from Lyman α cooling, H_2 rovibrational line cooling, fine structure emission from C II and O, and rotational line emission from CO. These processes are modelled using the prescription developed in Glover & Mac Low (2007a,b), Glover et al. (2010) and Glover & Clark (2012). The chemical network therefore follows the abundances of five key chemical species: H I, H II, H_2, C II, and CO. For the formation of molecular hydrogen and CO, the effects of dust shielding and molecular (self-)shielding are included using the TREECOL algorithm of Clark, Glover & Klessen (2012). Full details of the implementation of these processes within FLASH 4 are described in Walch et al. (2014) and Wünsch et al. (in preparation).

In hot gas, the excitation of helium and of partially ionized metals (e.g. O VI) becomes important. The contribution to the cooling rate from these processes is computed from the cooling rates of Gnat & Ferland (2012), which assume that the atoms and ions are in collisional ionization equilibrium. However, we explicitly follow the hydrogen ionization state since non-equilibrium effects are noticeable for gas at temperatures around 10^4 K (see e.g. Walch et al. 2011; Micic et al. 2013).

Diffuse heating from the photoelectric effect, cosmic rays, and X-rays is included following the prescriptions of Glover et al. (2010) and Glover & Clark (2012). We assume a constant radiation field where the photoionization from point sources is neglected. The far-UV interstellar radiation field is $G_0 = 1.7$ (Habing 1968; Draine 1978), while the cosmic ray ionization rate of H I is $\zeta = 3 \times 10^{-17}$ s^{-1}. For the X-ray ionization and heating rates, we use the values of Wolfire et al. (1995). The (constant) dust-to-gas mass ratio is set to 10^{-2}. We assume standard solar ratio of hydrogen to helium and solar metallicity with abundances $x_{\rm O,Si} = 3.16 \times 10^{-4}$, $x_{\rm SiII} = 1.5 \times 10^{-5}$ (Sembach et al. 2000), and $x_{\rm C,tot} = 1.41 \times 10^{-4}$. At $t = 0$, the gas has an ionization fraction of 0.1.

2.3 Initial turbulent stirring

At first, the gas is stirred with an Ornstein–Uhlenbeck random process (Eswaran & Pope 1988) with dimensionless wavenumbers $k = 1$–2, where $k = 1$ corresponds to the box side, L. The phase turnover time is $t_{\rm drive} = 25$ Myr, which corresponds to one crossing time for the warm gas. We distribute the turbulent energy on to solenoidal and compressive modes, using a 2:1 ratio. At every time-step, the total energy input is adjusted such that we obtain a global, mass-weighted, 3D root-mean-square (rms) velocity that is roughly constant at $v_{\rm 3D,rms} = 10$ km s^{-1}. We stir the gas for one crossing time (25 Myr) in order to generate a turbulent two-phase medium before the onset of SN driving (see also Walch et al. 2011).

2.4 SN driving

After 25 Myr, the artificial turbulent driving is stopped. Instead, we initialise SN explosions at a fixed rate, which we adjust to the mean box mass density ρ_i. We compute the gas surface density of the box as $\Sigma_{\rm gas} = \rho_i L$. The KS relation (Kennicutt 1998):

$$\frac{\Sigma_{\rm SFR}}{{\rm M}_\odot {\rm yr}^{-1} {\rm kpc}^{-2}} = 2.5 \times 10^{-4} \left(\frac{\Sigma_{\rm gas}}{{\rm M}_\odot {\rm pc}^{-2}} \right)^{1.4}, \tag{1}$$

relates the total gas surface density $\Sigma_{\rm gas} = \Sigma_{\rm HI+H_2}$ to a typical star formation rate (SFR) surface density. For a conventional stellar initial mass function (e.g. Salpeter 1955), approximately 100 M$_\odot$ of gas that collapses into stars produces on average only one massive star, which will explode as an SN Type II at the end of its lifetime. Hence, we only consider Type II SNe and neglect the additional contribution from Type Ia SNe, which is $\sim$15 per cent of the total SN rate in the Galaxy (Tammann, Loeffler & Schroeder 1994). With this information we compute the SN rate, $\dot{N}_{\rm SN,KS}$, for every n_i as

$$\frac{\dot{N}_{\rm SN,KS}}{\rm Myr} = \frac{\Sigma_{\rm SFR}}{{\rm M}_\odot {\rm Myr}^{-1} {\rm pc}^{-2}} \times 10^{-2} \frac{L^2}{{\rm pc}^2}. \tag{2}$$

The SN rate derived in this way is afflicted with uncertainties of at least a factor of 2. For this reason, we vary the SN rate by a factor of 2 for a number of initial densities. We list $\dot{N}_{\rm SN}$ for each density in Table 1.

2.5 SN energy and momentum input

For the majority of our simulations, each SN injects $E_{\rm SN} = 10^{51}$ erg of thermal energy into the ISM. We distribute this energy within a sphere with radius $R_{\rm inj}$. The radius of the injection region is adjusted such that it encloses 10^3 M$_\odot$ of gas, but we require $R_{\rm inj}$ to be resolved with a minimum of four cells:

$$R_{\rm inj} = \begin{cases} \left(\frac{3}{4\pi} \frac{10^3 \, {\rm M}_\odot}{\overline{\rho}} \right)^{1/3} & \text{if } R_{\rm inj} \geqslant 4\Delta x \\ 4\Delta x & \text{if } R_{\rm inj} < 4\Delta x, \end{cases} \tag{3}$$

where $\overline{\rho}$ is the mean density within the injection region. Here, we present an SN model that combines the injection of thermal energy and momentum and which adjusts to the local environment of each SN explosion (see Section 3.7).

2.5.1 Thermal energy input

If the SNe are resolved, we inject all of the SN energy in the form of thermal energy. Typically, the gas within $R_{\rm inj}$ is then heated up to $\approx 10^6$–10^7 K, which corresponds to a local sound speed $c_{\rm s}$ of a few hundred km s^{-1}. The associated pressure increase causes a Sedov–Taylor blast wave to expand into the ambient ISM. We decrease the time-step according to a modified Courant–Friedrichs–Lewy (CFL) condition to capture the dynamics of the blast wave:

$$\Delta t = C_{\rm CFL} \frac{\Delta x}{\max(|v| + c_{\rm s})}. \tag{4}$$

2.5.2 Momentum input

In case of high densities within the injection region, the Sedov–Taylor phase of the SN remnant is unresolved. The mass within the

injection region is high ($M_{inj} > $ few $\times 10^3$ M$_\odot$), and therefore the thermal energy input would result in an effective temperature below 10^6 K:

$$T_{i,SN} = (\gamma - 1)\frac{E_{SN}}{M_{inj}}\frac{\mu m_p}{k_B} < 10^6 \text{ K}, \quad (5)$$

where γ is the polytropic index, μ the mean molecular weight, m_p the proton mass, and k_B the Boltzmann constant.

The cooling rate is a non-linear function of the gas temperature. At $T < 10^6$ K, the injected energy is almost instantaneously lost due to strong radiative cooling. The employment of a limited mass and/or spatial resolution may then lead to overcooling, which is a well-known problem in galaxy simulations (e.g. Stinson et al. 2006; Creasey et al. 2011; Gatto et al. 2013). Many different solutions have been put forward to address the problem of unresolved SNe: switching off cooling for a certain time after the explosion (e.g. Thacker & Couchman 2000); clustering of massive stars to develop superbubbles (e.g. Shull & Saken 1995; Krause et al. 2013; Keller et al. 2014; Sharma et al. 2014); or momentum rather than energy input (e.g. Kim, Kim & Ostriker 2011; Shetty & Ostriker 2012). Of course one could just increase the resolution (see Section 3.8).

We choose a momentum input scheme for unresolved SNe, which is based on Blondin et al. (1998). For each explosion, we first calculate the radius of the bubble at the end of the Sedov–Taylor phase (Blondin et al. 1998)

$$R_{ST} = 19.1 \left(\frac{E_{SN}}{10^{51} \text{ erg}}\right)^{5/17} \left(\frac{\bar{n}}{\text{cm}^{-3}}\right)^{-7/17} \text{ pc}, \quad (6)$$

where $\bar{n}$ is the mean number density within the injection region. If $R_{ST} < 4\Delta x$, then we inject momentum rather than thermal energy (see also Hopkins et al. 2014). The momentum is computed from (Blondin et al. 1998)

$$p_{ST} = 2.6 \times 10^5 \left(\frac{E_{SN}}{10^{51} \text{ erg}}\right)^{16/17} \left(\frac{\bar{n}}{\text{cm}^{-3}}\right)^{-2/17} \text{ M}_\odot \text{ km s}^{-1}. \quad (7)$$

We deposit this momentum to the flattened density distribution within the injection region by adding the corresponding velocity of

$$v_{inj} = \frac{p_{ST}}{M_{inj}}, \quad (8)$$

where v_{inj} points radially outwards. In addition, we increase the temperature of the injection region to 10^4 K. This guarantees that, despite the significant energy losses, the momentum input is accounted for.

This method has two caveats. (i) The momentum of an SN bubble can still increase during the pressure-driven snowplough phase (Cioffi, McKee & Bertschinger 1988), which is not included in this model. (ii) Due to the injection of transonic or subsonic motions, high Mach number shocks are not created and little to no hot gas is produced. Therefore, the momentum input given in equation (7) is a lower limit.

Recent results by Kim & Ostriker (2014, see also Martizzi, Faucher-Giguère & Quataert 2014; Simpson et al. 2014) indicate that the final momentum driven by a single SN explosion can be captured (within 25 per cent of the expected value from high resolution, sub-pc simulations) under the conditions: (i) $R_{ST} > 3 R_{inj}$ and (ii) $R_{ST} > 3 \Delta x$. This is roughly insensitive to the ambient medium density distribution. As a result, the impact of SNe exploding in density peaks might be underestimated even when $T_{i,SN} > 10^6$ K for thermal energy injection. In Section 3.8, we compare these requirements with our results at different resolutions.

Table 2. List of all simulations. From left to right: name of the simulation; initial number density of the box n_i; SN rate $\dot{N}_{SN}$; driving mode: pure random (R), pure peak (P) or mixed (M).

Name	n_i (cm^{-3})	$\dot{N}_{SN}$ (Myr^{-1})	Driving	Note
R-$n_{0.5}$	0.5	1.2	R	
R-n_1	1	3	R	
R-n_{1-}	1	1.5	R	
R-n_{1+}	1	6	R	
R-n_3	3	14	R	
R-n_{3-}	3	7	R	
R-n_{3+}	3	28	R	
R-n_{10}	10	77	R	
R-n_{10-}	10	38.5	R	
R-n_{10+}	10	154	R	
R-n_{30}	30	360	R	
R-n_{30-}	30	180	R	
R-n_{30+}	30	720	R	
P-$n_{0.5}$	0.5	1.2	P	
P-n_1	1	3	P	
P-n_3	3	14	P	
P-n_{10}	10	77	P	
M10-n_3	3	14	M	$f_{peak} = 10$
M20-n_3	3	14	M	$f_{peak} = 20$
M30-n_3	3	14	M	$f_{peak} = 30$
M40-n_3	3	14	M	$f_{peak} = 40$
M50-n_3	3	14	M	$f_{peak} = 50$
M60-n_3	3	14	M	$f_{peak} = 60$
M70-n_3	3	14	M	$f_{peak} = 70$
M80-n_3	3	14	M	$f_{peak} = 80$
M90-n_3	3	14	M	$f_{peak} = 90$
P-C-n_3	3	14	P	CM
M50-C-n_3	3	14	M	CM $f_{peak} = 50$
R-HR-n_3	3	14	R	$\Delta x = 1$ pc
P-HR-n_3	3	14	P	$\Delta x = 1$ pc

Note: combined model with thermal energy and momentum input (CM).

2.5.3 SN positions and simulations

We will show that the positioning of the SNe relative to the gas density distribution changes the structure of the ISM. Therefore, we choose three different schemes to place the SNe: (i) random driving (runs R-n_i), (ii) peak driving (runs P-n_i), i.e. the current SN is placed on the global density maximum at the time, and (iii) a mixture of the two, i.e. mixed driving (runs Mf-n_i), with a fixed ratio f_{peak} of peak to total SNe.

We carry out a number of simulations with different driving schemes and densities, which we summarize in Table 2. By default, we choose random driving. For this driving scheme, we run five simulations with $\dot{N}_{SN,KS}$ for $n_i = 0.5, 1, 3, 10, 30$ cm^{-3} and eight for $n_i = 1, 3, 10, 30$ cm^{-3} with half ($\dot{N}_{SN,-}$) and twice the KS SN rate ($\dot{N}_{SN,+}$). In addition, we perform four simulations ($n_i = 0.5, 1, 3, 10$ cm^{-3}) with peak driving. For $n_i = 3$ cm^{-3}, we carry out nine simulations using mixed driving with different values of f_{peak}.

We investigate the applicability of the combined model of thermal energy and momentum injection using two simulations with $n_i = 3$ cm^{-3} and $f_{peak} = 100$ per cent (P-C-n_3) and 50 per cent (M50-C-n_3). Finally, we run two simulations for $n_i = 3$ cm^{-3} at a higher resolution (with $\Delta x = 1$ pc). These runs are called R-HR-n_3 for random and P-HR-n_3 for peak driving.

2.6 Simulation analysis

The simulations are stopped once an approximate chemodynamical equilibrium is reached, i.e. the mass distribution of the different chemical species stays roughly constant. This is typically the case after 100–200 Myr (note that 25 Myr was the initial crossing time), depending on the initial box density and SN rate. We discuss the properties of the resulting ISM for different initial densities, driving schemes, and resolution towards the end of the simulations. In particular, we focus on four quantities:

(i) the distribution of gas mass among ionized, neutral, and molecular hydrogen;

(ii) the gas pressure in different temperature regimes;

(iii) the VFFs of gas within the different temperature regimes; and

(iv) the observable velocity dispersion.

We compute every quantity by averaging over the final 5 Myr of each simulation in order to reduce statistical errors. In Appendix A, we show the full time history for three simulations with $n_i = 3 \, \text{cm}^{-3}$ using random and peak driving.

To compare with velocity dispersions observed in H I and Hα, we compute the mass-weighted, one-dimensional velocity dispersion, $\sigma_{\text{avg 1D}}$. We first compute the 1D dispersion for H I and Hα along the x-, y-, and z-directions for each simulation:

$$\sigma_{j,k,\text{turb}} = \left(\frac{\sum_i (v_{i,k} - \bar{v}_k)^2 \, m_{i,j}}{M_{j,\text{tot}}} \right)^{1/2} , \qquad (9)$$

where j indicates the chemical species (H I or Hα), i is the cell index, v_i is the velocity of the cell, and $\bar{v}$ is the average velocity in the respective direction k. m_j is the mass of species j in cell i, and $M_{j,\text{tot}}$ is the total mass of species j. We then average over all three directions and receive a mean, one-dimensional velocity dispersion:

$$\sigma_{j,\text{turb}} = \frac{1}{3} \sum_{k=1}^{3} \sigma_{j,k,\text{turb}}. \qquad (10)$$

H I velocity dispersion. for H I the intensity is proportional to the number of emitters (e.g. Rohlfs & Wilson 1996). Therefore, the H I mass is a good proxy for the total radiation flux, i.e. $M_j \propto L_j$, and the resulting velocity dispersion, $\sigma_{\text{H I,turb}}$, can be considered as an intensity-weighted velocity dispersion.

Hα velocity dispersion. for Hα, the mass of ionized hydrogen is not a good estimate of the Hα intensity, since the emission decreases with increasing temperature. Here, we compute the Hα flux from two contributions, namely the recombination of ionized hydrogen and collisional excitation from the ground state to level $n = 3$. We have to neglect the contribution from H II regions around young massive stars since these are not treated in the simulations. Collisional excitations to $n > 3$ represent a negligible contribution to the total Hα emission since transitions to these levels are significantly less likely (Anderson et al. 2000, 2002, but see also Péquignot & Tsamis 2005 and references therein). We compute $m_{\text{H}\alpha}$ ($dL_{\text{H}\alpha}$) and $M_{\text{tot,H}\alpha}$ ($L_{\text{tot,H}\alpha}$), required in equation (9), following the emissivity calculations for recombination and collisional excitation of Draine (2011), Dong & Draine (2011), and Kim et al. (2013b) (but see also Aggarwal 1983):

$$dL_{\text{H}\alpha,\text{R}} \propto T_4^{-0.942 - 0.031 \ln(T_4)} n_e n_{\text{H II}} dV , \qquad (11)$$

$$dL_{\text{H}\alpha,\text{C}} \propto \frac{\Gamma_{13}(T_e)}{\sqrt{T_e}} e^{\frac{-12.1\text{eV}}{k_B T_e}} n_e n_{\text{H I}} dV , \qquad (12)$$

where $T_4 = T/10^4$ K, T_e is the electron temperature, n_j is the number density of species j in cm^{-3}, dV is the zone volume, and

$$\Gamma_{13}(T_e) = 0.35 - 2.62 \times 10^{-7} T_e - 8.15 \times 10^{-11} T_e^2$$
$$+ 6.19 \times 10^{-15} T_e^3. \qquad (13)$$

We apply equation (12) only for cells with temperatures $4000 < T < 25\,000$ K assuming $T_e = T$. We only consider this temperature range because emission at $T < 4000$ K will be negligible, while we expect to find very little atomic hydrogen at $T > 25\,000$ K. We also assume $n_e = n_{\text{H II}}$, which results in an ~10 per cent error at most in regions where helium is ionized.

We approximate the gas to be optically thin to the Hα and H I emission. Although this assumption might lead to a poor estimate of the line intensities, we do not expect major absorption features except in cold and dense H I clouds. In this case H I self-absorption could also play a non-negligible role. However, as we will see in the next sections, most of the dense clumps in our models are composed of H$_2$, with only a small mass fraction of atomic gas in the outer shells.

Thermal component. we include thermal broadening by adding a mass-weighted thermal velocity

$$\sigma_{j,\text{therm}} = \left(\frac{\sum_i v_{i,\text{therm}}^2 \, m_{i,j}}{M_{j,\text{tot}}} \right)^{1/2} , \qquad (14)$$

where $v_{i,\text{therm}} = (2k_B T_i / \mu_i)^{1/2}$ with T_i being the temperature, and μ_i the mean mass per particle in cell i. We assume that all species within a cell have the same temperature, which can cause small errors in the thermal velocity estimate. The resulting total velocity dispersion is

$$\sigma_{\text{avg 1D},j} = \left(\sigma_{j,\text{turb}}^2 + \sigma_{j,\text{therm}}^2 \right)^{1/2} . \qquad (15)$$

3 RESULTS AND DISCUSSION

3.1 Energy input

In Fig. 1, we show the cumulative energy input as a function of time for artificial turbulent driving (solid lines) and SN driving (dashed lines) with an SN rate derived from the KS relation, for initial densities $n_i = 0.5$, 3, and $10 \, \text{cm}^{-3}$. We point out that the energy
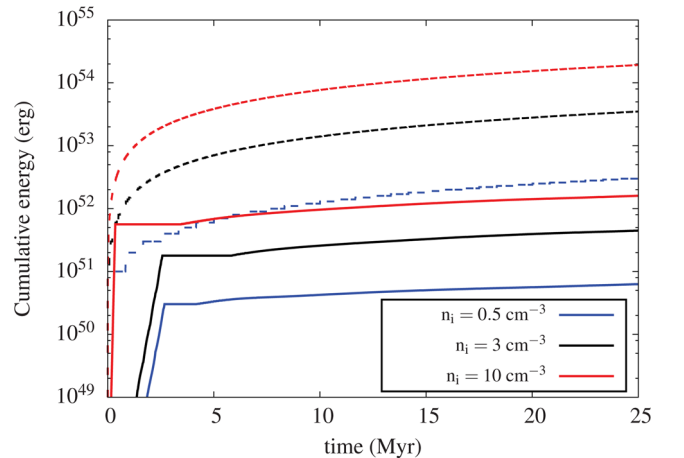

Figure 1. Cumulative energy injected in the first 25 Myr of artificial (solid lines, $t = 0$–25 Myr) and SN driving (dashed lines, $t = 25$–50 Myr) for different n_i.
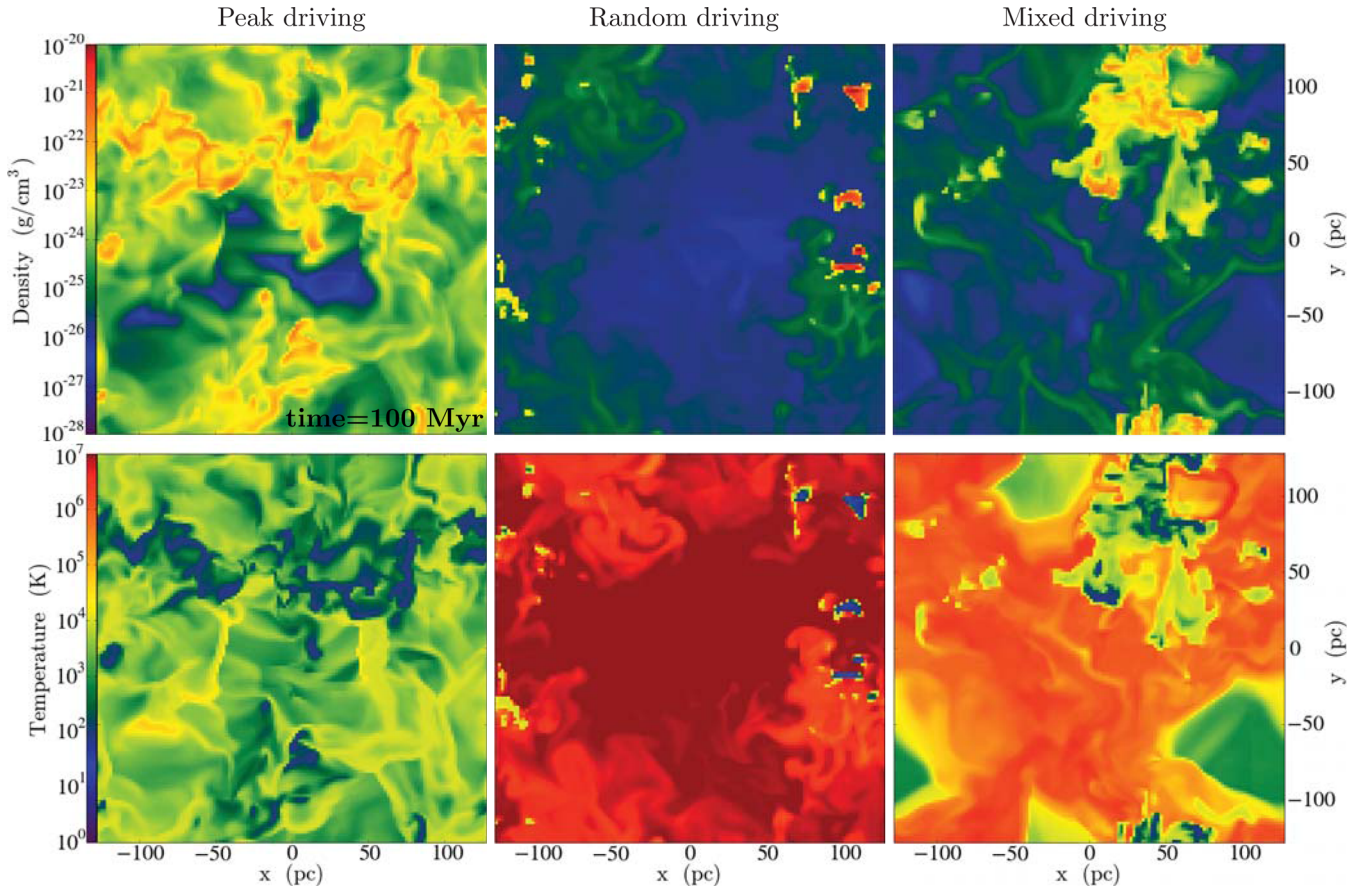
Figure 2. Density (top row) and temperature (bottom row) slices for three runs with initial density $n_i = 3\,\mathrm{cm}^{-3}$ and SN rate drawn from the KS relation $\dot{N}_{\mathrm{SN,KS}}$. From left to right, we show runs P-n_3 (peak driving), R-n_3 (random driving), and M50-n_3 (mixed driving with $f_{\mathrm{peak}} = 50$ per cent) at $t = 100$ Myr.

input from artificial driving necessary to maintain a constant 3D, mass-weighted, rms velocity of $v_{\mathrm{3D,rms}} = 10\,\mathrm{km\,s}^{-1}$ (corresponding to a one-dimensional velocity dispersion of $\sim$5–6 km s^{-1}) is always about two orders of magnitude lower than the energy input in the corresponding SN-driven box. Nevertheless, we will see that SN driving is inefficient in terms of turbulence driving. Therefore, even though the energy input is high, the resulting, average, one-dimensional velocity dispersions in cold H I gas stay below $10\,\mathrm{km\,s}^{-1}$.

3.2 Impact of SN positioning

We start from the artificially stirred, turbulent box at different densities at $t_{\mathrm{drive}} = 25$ Myr. We then evolve the simulations with SN driving at different rates and positioning of the SNe relative to the dense gas.

Density and temperature distribution. in Fig. 2, we compare the density and temperature structure of the ISM for three runs with $n_i = 3\,\mathrm{cm}^{-3}$ and $\dot{N}_{\mathrm{SN,KS}}$ at $t = 100$ Myr, using peak driving (run P-n_3, left-hand column), random driving (run R-n_3, middle column), and mixed driving (run M50-n_3, i.e. mixed driving with $f_{\mathrm{peak}} = 50$ per cent, right-hand column). The SN rate is the same and the huge differences in the ISM structure are solely due to the positioning of the SNe. For peak driving, the box is filled with warm and cold gas, which is distributed in filaments and extended clouds. There is little to no hot gas present. In the case of random driving, on the other hand, most of the box is filled with hot gas, while the

cold gas is concentrated in small and dense clumps. The mixed driving case with an equal contribution from random and peak driving lies in between the other two cases. Gas at $T \gtrsim 10^6$ K occupies the majority of the box volume, but the cold and warm phases are located not just in massive clumps, but also in extended filamentary complexes.

Density probability distribution functions. in Fig. 3, we show the volume-weighted probability distribution functions (PDFs) of density for the initial condition derived from artificial turbulence stirring at $t_{\mathrm{drive}} = 25$ Myr (black line) and for the three different driving modes at $t = 100$ Myr. For artificial driving at an rms velocity of 10 km s^{-1}, we find a broad PDF which can be interpreted as two overlapping lognormal distributions. The medium does not consist of two distinct warm and cold phases. A significant fraction of the gas lies far from the equilibrium curve due to turbulent motions (e.g. Walch et al. 2011, but see also Vázquez-Semadeni, Gazol & Scalo 2000; Micic et al. 2013; Saury et al. 2014). For peak driving (blue line), the PDF roughly coincides with the one for artificial driving at high densities, but with a more extended tail towards low densities. In the case of random driving (red line), the distribution has a strong peak at low densities ($\rho \sim$ few $\times\,10^{-26}$ g cm^{-3}), which corresponds to the hot, overpressured phase, followed by two subsequent peaks at higher densities. The maximum density reached is well above the ones produced by other driving modes. Since most of the volume is filled with hot gas, the volume-weighted PDF is dominated by a single peak at low densities. Mixed driving (green line) displays an intermediate distribution between random and peak driving with
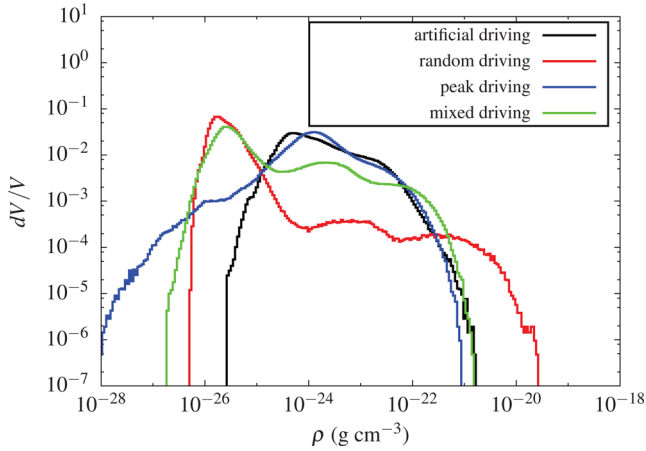
Figure 3. Volume-weighted density PDFs for different driving modes, i.e. random (red line), peak (blue line), and 50 per cent mixed driving (green line), for the $n_i = 3\,\mathrm{cm}^{-3}$ runs at $t = 100$ Myr. In addition, we show the initial condition from artificial stirring at $t_{\mathrm{drive}} = 25$ Myr (black line).

three broad peaks. This is typical for a turbulent three-phase ISM consisting of cold, warm, and hot gas, with significant contributions from each component (e.g. Gent et al. 2013).

Phase diagrams. in Fig. 4, we show exemplary ρ–T and ρ–P phase diagrams for random and peak driving, where the mass distribution is colour-coded. In the random driving case (top row), the gas is moved to high pressures $P/k_{\mathrm{B}} \gtrsim 10^4\,\mathrm{K\,cm}^{-3}$, which is above the

mean pressure in the Milky Way (e.g. Jenkins & Tripp 2011). A small fraction of the gas reaches high temperatures $T > 10^6$ K; this gas occupies virtually all of the volume, as shown in Fig. 3. This hot, high-pressure gas pushes the majority of the mass into the cold, dense phase (see Section 3.3). The cold, high-density tail lies slightly below the equilibrium curve. A likely explanation is that at high density, the cold gas is efficiently shielded against the far-UV interstellar radiation field. Since the equilibrium values are computed without considering this mechanism, the densest component has a lower equilibrium pressure and temperature in this density range.

On the other hand, in the peak driving case (bottom row) a two-phase medium, with warm and cold gas in approximate pressure equilibrium, is formed. The densest component actually lies slightly above the equilibrium curve due to the continuous heating of the densest gas parcels by SN shocks. However, these simulations contain little to no hot gas, as the SNe, which explode only in dense environments, fail to effectively heat the gas (see Section 3.5). The maximum densities reached in simulations with peak driving are one to two orders of magnitude smaller than in the random driving case since, by construction, peak driving removes the densest component of the medium and highly overpressured hot regions are not present in this case.

Summary. we may summarize the impact of the different SN positioning (see Figs 2 and 4) as follows: in the case of random driving, most SNe are placed in positions where their energy can be efficiently transferred to the ISM. In the case of peak driving, the SNe explode in dense gas, which may promptly radiate a large fraction
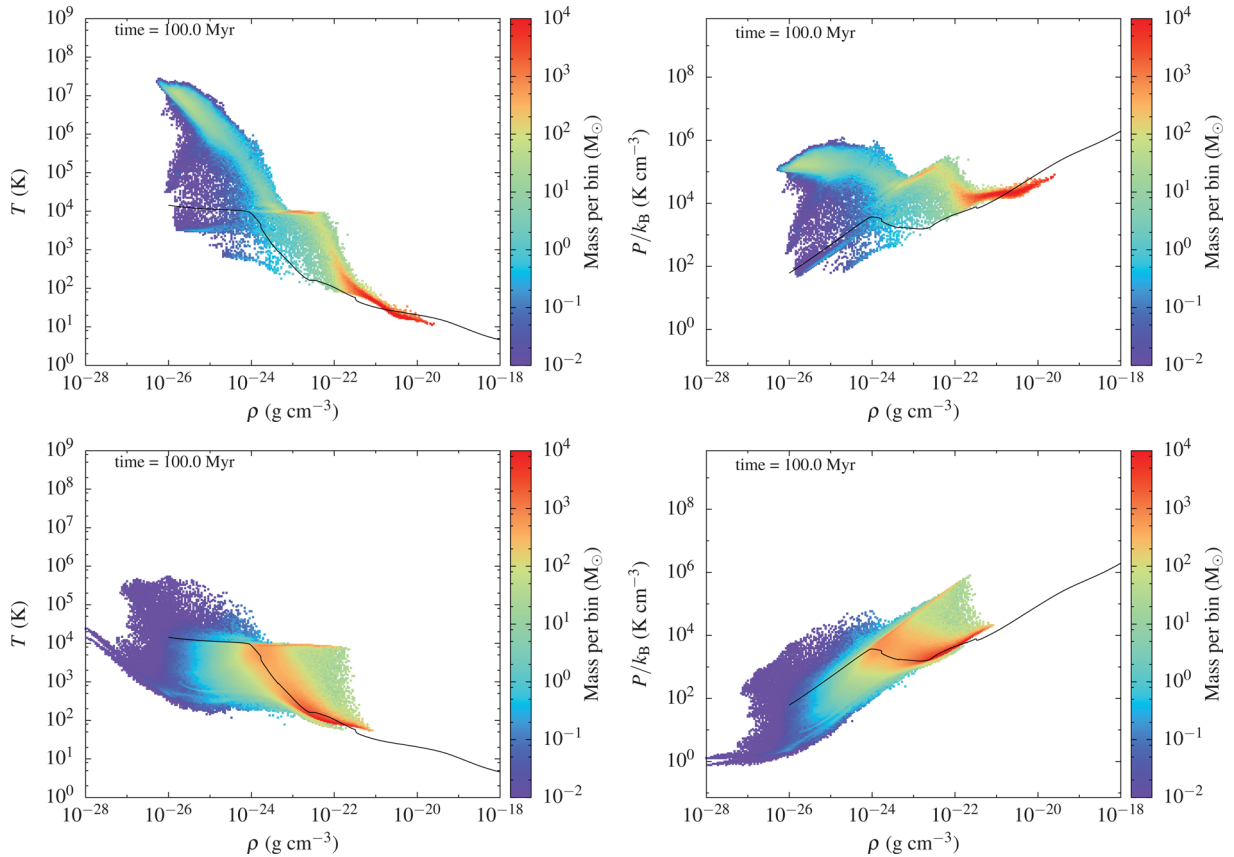

Figure 4. Density–temperature (left) and density–pressure (right) phase diagrams for two simulations with initial density $n_i = 3\,\mathrm{cm}^{-3}$ and $\dot{N}_{\mathrm{SN,KS}}$ at $t = 100$ Myr. We colour-code the mass distribution. The first row shows run R-n_3 (random driving), while the second row shows run P-n_3 (peak driving). The solid lines show where radiative cooling and diffuse radiative heating reach equilibrium.

of the inserted energy. The higher the fraction of random SNe, the more efficiently energy is injected, which increases the thermal gas pressure and increases the chance to end up in a thermal runaway regime, as discussed in the next subsection. In Section 3.6, we explore this transition in simulations with different f_{peak}.

3.3 Thermal runaway

The high pressure reached in our models results in the equilibrium between heating and cooling lying not in the regime near $P/k_B \sim 10^3 \, \text{K cm}^{-3}$ where a two-phase medium is possible, but rather on the cold branch of the equilibrium curve, where balance between heating and cooling can only be reached at low temperatures and high densities. This explains why virtually all the mass lies at high density ($n > 100 \, \text{cm}^{-3}$) and low temperature ($T < 200 \, \text{K}$). As a result, we move from the classic paradigm of a two-phase medium in pressure equilibrium towards a scenario in which only the cold phase survives, consistent with the picture of Wolfire et al. (1995) for high heating (far-UV interstellar field) rates. The cooling times in the remaining rarefied gas are long, since radiative cooling is proportional to n^2 and drops significantly for temperatures above 10^6 K (Raymond, Cox & Smith 1976). As a result, almost all of the volume is occupied by gas with low density and $T > 10^6$ K, whose cooling time far exceeds the dynamical time of the system: the third phase of the three-phase medium (McKee & Ostriker 1977). This picture is consistent with the findings of Scannapieco, Gray & Pan (2012), who use hydrodynamical simulations of artificially-driven turbulence in a stratified disc to mimic the impact of stellar feedback. They find that, for turbulent one-dimensional velocity dispersions $\gtrsim 35 \, \text{km s}^{-1}$, large fractions of gas are continuously heated and unable to cool within a turbulent crossing time. This process leads to powerful outflows and compression of cold gas. In the thermal runaway regime, our simulations behave in a similar way, as energy is directly deposited into a hot, high-pressure medium, with a resulting one-dimensional velocity dispersion of the hot phase well above the critical value of $35 \, \text{km s}^{-1}$.

The high pressures reached in the thermal runaway regime marks a clear distinction from the classic picture of McKee & Ostriker (1977). In that model, an SN remnant expands into a medium characterized by the presence of many evenly-distributed, small, two-phase clouds having cold cores surrounded by warm envelopes. The passage of the SN blast wave heats and destroys these clouds, sweeping them up into a dense shell. This dense shell cools and slows down during the radiative phase, and the remnant ceases to exist when it reaches pressure equilibrium with the ambient medium. For thermal runaway, however, SNe go off in a hot, high-pressure environment, while isolated cold clouds lie far from the explosion position. Well before the end of the Sedov–Taylor phase, the remnants reach pressure equilibrium with the hot gas and deposit their energy into the medium without any significant radiative loss.

In this environment heating cannot be balanced by radiative cooling. In our periodic box, within which there is no vertical stratification to allow an atmosphere to evolve into hydrostatic equilibrium with a galactic potential, the hot gas pressure can only be set by the balance between cooling and heating. Random driving thus pushes the system towards a thermal runaway regime, where the hot gas contains most of the energy, while the majority of the box mass is stored in the coldest phase without the possibility to return to a system with a significant warm phase ($T \sim 10^4$ K). Cold gas is not formed from a two-phase medium, but instead cools directly to the cold branch of the equilibrium curve, forming high-density clumps with small VFF. The cold clumps are produced by compression
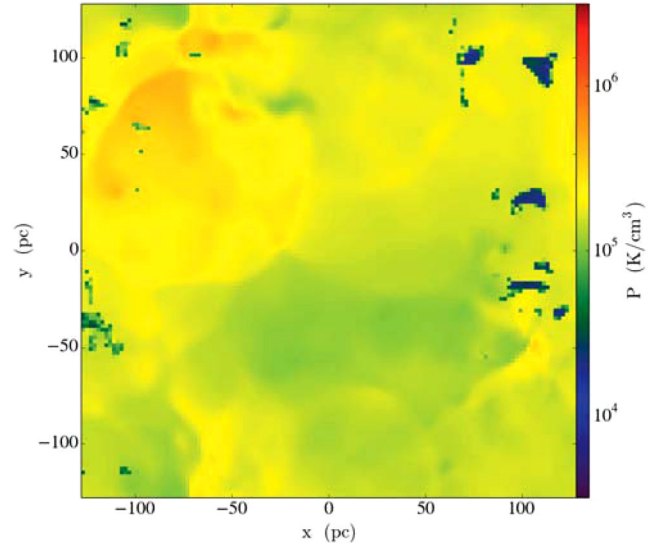

Figure 5. Pressure slice for the random driving run with initial density $n_i = 3 \, \text{cm}^{-3}$ and $\dot{N}_{SN,KS}$ at $t = 100$ Myr (see also the central column of Fig. 2).

waves coming from the hot, high-pressure gas. This mechanism causes an efficient and fast conversion from warm, atomic gas to molecular. These clumps are resolved by so few zones that they cannot reach high enough densities to remain in pressure equilibrium with the background. As a result, cold clouds at low pressures are embedded into a hot, high-pressure environment. This numerically caused jump in pressure can reach about one order of magnitude (see Fig. 5 for the pressure distribution in run with $n_i = 3 \, \text{cm}^{-3}$ and $\dot{N}_{SN,KS}$). Therefore, we must treat the interior properties of the clouds as limits at low density and velocity dispersion, rather than converged values.

3.4 Random driving at different SN rates

In this section, we discuss the properties of the ISM forming in runs R-n_i with randomly placed SNe and different initial densities n_i. The SN rates are adjusted to the given n_i (see Section 2.4). We perform three simulations with different SN rates for almost every n_i using $\dot{N}_{SN,KS}$, and $\dot{N}_{SN,-}$ and $\dot{N}_{SN,+}$, where the SN rate is decreased/increased by a factor of 2, respectively (see also Table 1). In Fig. 6, we compare the different simulations. We plot the mass in ionized, atomic, and molecular hydrogen (top-left panel), the pressure in three different temperature regimes, which are representative for the cold, warm ionized, and hot phase of the ISM (top right), the VFF in different temperature phases (bottom left), and the velocity dispersion of the gas in H I and Hα (bottom right) towards the end of each simulation. To guide the eye, we connect the simulations with equal n_i but different SN rate.

Chemical composition. we follow the chemical evolution of the gas, including the formation of molecular hydrogen, taking into account the effects of dust shielding and molecular (self-) shielding. We find that the mass in ionized hydrogen is always below 10 per cent and decreasing for increasing box density. For low densities ($n_i \lesssim 3 \, \text{cm}^{-3}$) most of the total mass is in atomic hydrogen. At higher densities ($n_i \gtrsim 3 \, \text{cm}^{-3}$) less than 50 per cent of the mass is in H I and the rest is in molecular hydrogen. Molecular hydrogen, which is organized in small, dense clumps (see Fig. 2),
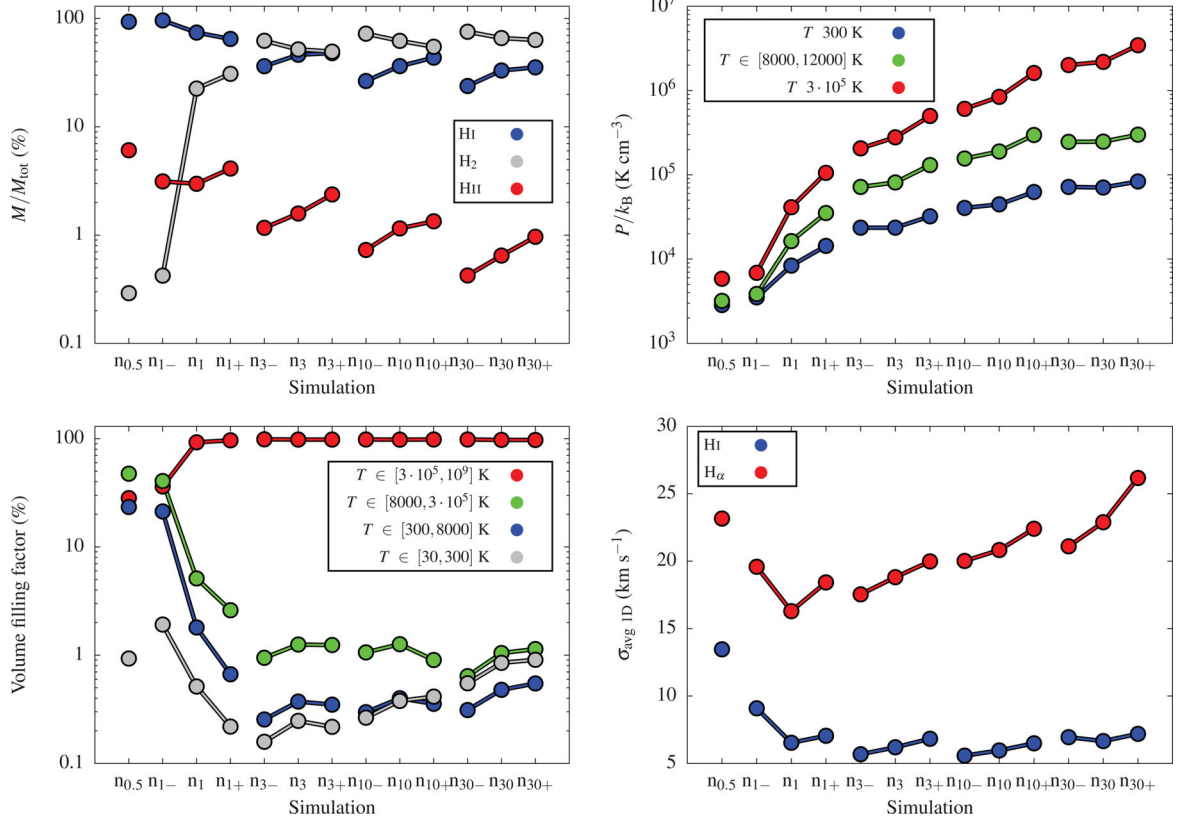
Figure 6. Average mass fractions (top left), pressures (top right), VFFs (bottom left), and 1D velocity dispersions (bottom right) with random driving for different initial densities n_i and SN rates. The index i represents the initial number density, while the $+$ and $-$ signs give the SN rate ($\dot{N}_{\mathrm{SN},+}$ and $\dot{N}_{\mathrm{SN},-}$). The values are averaged over the last 5 Myr (Section 2.6). The different lines connect simulations with same n_i but different SN rate.

dominates the mass budget at high densities and SN rates (up to 80 per cent of the total mass is in form of H_2 at $n_i = 30\,\mathrm{cm}^{-3}$).

Gas pressure. we compute the average pressure in three different temperature regimes: (i) for the stable cold phase at $T \leq 300$ K; (ii) for the stable warm phase at $8000 \leq T \leq 12\,000$ K; and (iii) for the hot phase at $T \geq 3 \times 10^5$ K. For $n_i \leq 1\,\mathrm{cm}^{-3}$ the medium is roughly in pressure equilibrium, but for higher densities and SN rates the pressures of the three phases diverge slowly as we get into the thermal runaway regime.

VFF. we show the VFFs of the gas in the bottom-left panel of Fig. 6. We distinguish four different temperature regimes: the cold phase at $30 \leq T < 300$ K; the warm atomic ISM at $300 \leq T < 8000$ K; the warm ionized medium at $8000 \leq T < 3 \times 10^5$ K; and the hot ionized medium at $T \geq 3 \times 10^5$ K. Only for two simulations, (R-$n_{0.5}$ and R-n_{1-}), are the VFFs close to what we expect for a Milky Way-type galaxy near the mid-plane (e.g. Kalberla & Dedes 2008; Kalberla & Kerp 2009), whereas the hot gas fills most of the volume at higher densities and/or SN rates.

We compare the VFFs of the hot ionized medium with the analytic prediction of McKee & Ostriker (1977). The volume occupied by SN remnants at random locations in a uniform medium, f, can be written as

$$f = 1 - e^{-Q} , \tag{16}$$

with porosity Q defined as

$$Q = 10^{-0.29} E_{51}^{1.28} S_{-13} \bar{n}^{-0.14} \tilde{P}_{04}^{-1.3} , \tag{17}$$

where E_{51} is the SN energy normalized to 10^{51} erg, S_{-13} is the SN rate in units of $10^{-13}\,\mathrm{pc}^{-3}\,\mathrm{yr}^{-1}$, $\bar{n}$ is the number density of the

ambient medium in cm^{-3}, and $\tilde{P}_{04} = 10^{-4} P_0/k_\mathrm{B}$, with P_0 and k_B ambient medium pressure and Boltzmann constant, respectively.

We find a reasonable agreement of the VFF for models R-$n_{0.5}$ and R-n_{1-}, where $f \sim 30$–40 per cent. However, the analytic model predicts lower hot gas VFFs for higher densities and SN rates such than the ones found in our higher SN rate simulations. Since $Q \propto \bar{n}^{1.26} \tilde{P}_{04}^{-1.3}$, f as derived from equations (16) and (17) is roughly constant, whereas the simulation shows it increasing towards unity in the thermal runaway regime.

H I and Hα velocity dispersion. in the bottom-right panel of Fig. 6, we show the velocity dispersions in H I, $\sigma_{\mathrm{avg\,1D}}(\mathrm{H\,I})$, and Hα, $\sigma_{\mathrm{avg\,1D}}(\mathrm{H\alpha})$. For $n_i \leq 1\,\mathrm{cm}^{-3}$ and, in particular, for low SN rates ($\dot{N}_{\mathrm{SN}} \lesssim 2\,\mathrm{Myr}^{-1}$), SNe are able to inject the observed level of turbulence in the H I gas, while $\sigma_{\mathrm{avg\,1D}}(\mathrm{H\,I}) \sim 5$–$7\,\mathrm{km\,s}^{-1}$ for $n_i > 1\,\mathrm{cm}^{-3}$. Due to the small size of most cold clumps, these values are a mixture of the clump-to-clump velocity dispersion and thermal broadening, rather than being a measure of the disordered motions within these clouds. For the Hα dispersion, we find a similar trend going from SN rates of $\dot{N}_{\mathrm{SN}} \lesssim 2\,\mathrm{Myr}^{-1}$ to slightly higher ones. First, $\sigma_{\mathrm{avg\,1D}}(\mathrm{H\alpha})$ drops from $\sim 24\,\mathrm{km\,s}^{-1}$ to $\sim 17\,\mathrm{km\,s}^{-1}$, but then it increases slowly with increasing box density and SN rate and is $\sim 26\,\mathrm{km\,s}^{-1}$ for $n_i = 30\,\mathrm{cm}^{-3}$ and high SN rates.

3.5 Peak driving versus random driving

We perform simulations using peak driving (runs P-n_i) at the same box densities and SN rates as in the corresponding runs with random driving (see Table 2). In Fig. 7, we show the resulting ISM properties with respect to the random driving case.
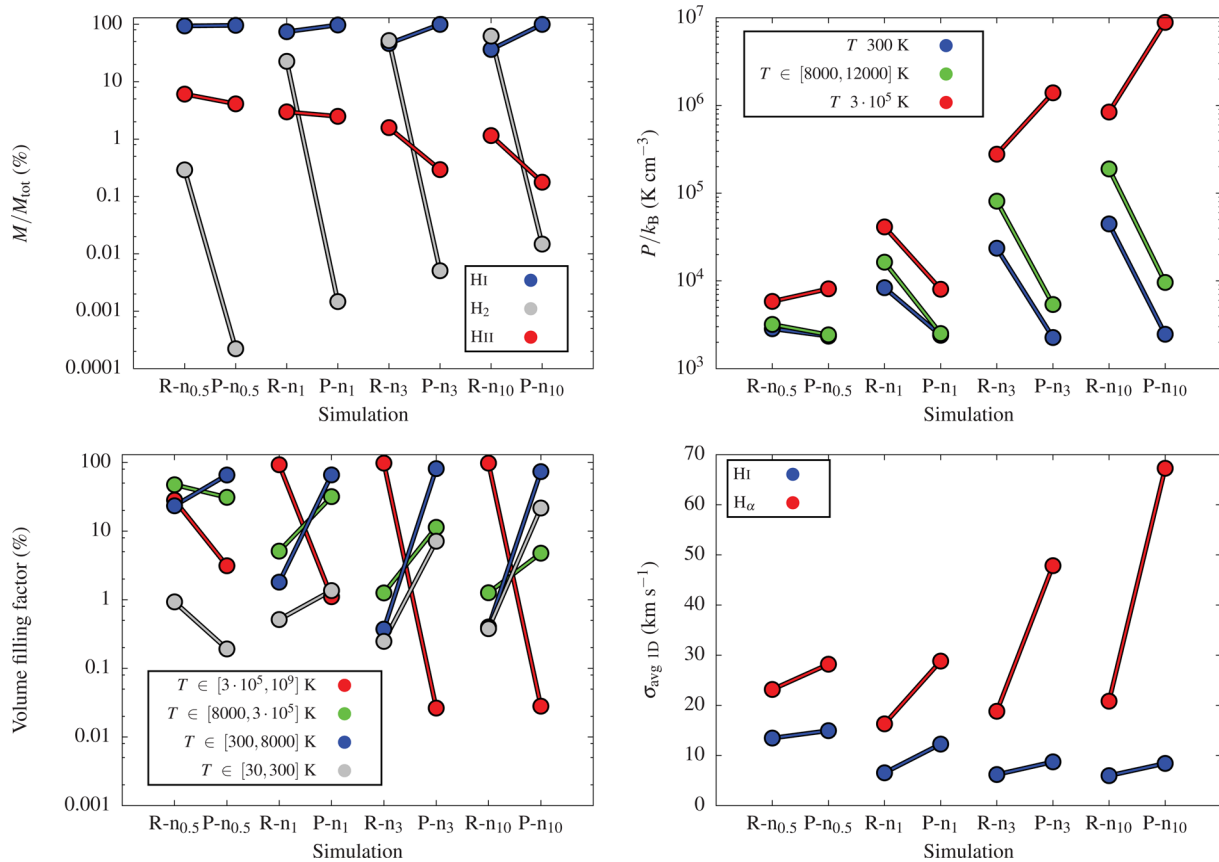
Figure 7. Average mass fractions (top left), pressures (top right), VFFs (bottom left), and 1D velocity dispersions (bottom right) with random (R) and peak (P) driving for different initial densities n_i, using the corresponding $\dot{N}_{\rm SN,KS}$. The lines connect simulations with equal n_i and SN rate but different driving modes (R or P).

Chemical composition. the peak driving runs are dominated by atomic rather than molecular gas. The H_2 mass fraction is low for two reasons: (i) the densest peaks are dispersed by SNe and, therefore, H_2 is locally dissociated; and (ii) the strong compressive SN shocks, which are widespread in the case of random driving, are localized in the immediate neighbourhood of the SN for peak driving. The destruction of molecular gas from peak SNe is broadly consistent with the findings of Hennebelle & Iffrig (2014) and Iffrig & Hennebelle (2014), where SNe exploding close to or within star formation sites can disperse cold and dense gas. In addition, the inefficient heating by peak SNe further reduces the small fraction of mass in the form of thermally ionized hydrogen.

Gas pressure. we find lower pressures for peak driving, in particular for the warm and cold gas components. However, the pressure of the hot phase ($T \geq 3 \times 10^5$ K) appears to be significantly higher (by a factor of ~ 10) in the case of peak driving at $n_i \geq 3$ cm^{-3}. This increase has to be interpreted in conjunction with the decreasing VFF of the hot gas at these densities. Since the SNe, which explode in high-density environments, are subject to strong radiative cooling, the high pressure reflects the young age of the SN remnants that do contribute to the hot phase.

VFF. peak driving does not produce a predominantly hot ISM. Instead, the VFF is highest for the warm and cold atomic phases. In particular, for low densities, a non-negligible contribution is also produced by the warm ionized medium, but the VFF of this component decreases with increasing density, similar to the case of random driving. In general, the absence of a significant hot phase reflects

the small sphere of influence of each peak SN, whose expansion is stopped early on due to strong radiative cooling.

H I and Hα velocity dispersion. In the case of peak driving, the H I velocity dispersion is slightly higher than for random driving. This is reasonable since the SNe deposit momentum into the cold gas. The velocity dispersion of the warm ionized gas as seen in Hα grows even more significantly up to 50–70 km s^{-1} for $n_i \geq 3$ cm^{-3}. As we have seen, the hot and warm ionized gas are found in the earliest stages of the SN remnants, which otherwise cool efficiently. Thus, the apparent high values of the Hα velocity dispersion stem from the integration over a number of isolated, compact, young SN remnants.

3.5.1 Discussion: Is peak driving realistic?

Fig. 7 shows that peak driving efficiently disperses cold gas. The SNe which, by choice, explode in the densest environments, are subject to strong radiative cooling. For this reason, peak driving fails to reproduce both the VFF of hot gas and the large molecular gas mass fractions characteristic of the Milky Way (Ferrière 2001). The absence of hot gas is also inconsistent with the expectation of SNe being responsible for the creation of a hot phase (McKee & Ostriker 1977).

We can conclude that pure peak driving does not reproduce realistic ISM conditions – probably because we neglect other important physical ingredients, such as clustering and stellar feedback mechanisms, i.e. pre-SN feedback like stellar winds and ionizing radiation
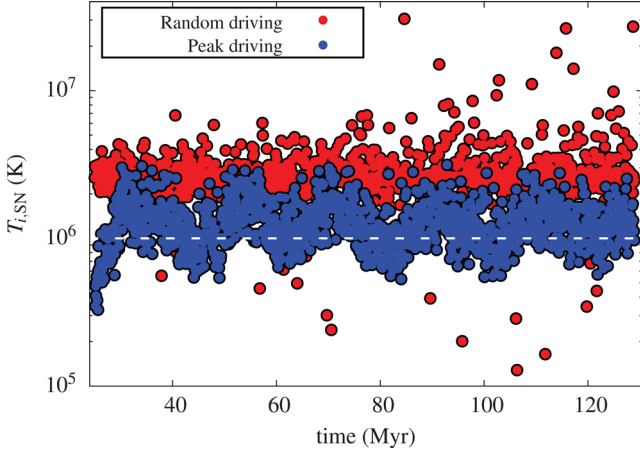
Figure 8. Initial temperature of SNe estimated from equation (5) for pure peak and random driving with $n_i = 3\,\mathrm{cm}^{-3}$ and $\dot{N}_{\mathrm{SN,KS}}$.

an unfavourable temperature regime, the cooling curve is steep and the heated SN gas can be cooled efficiently.

Fig. 8 shows the approximate initial temperatures (from equation 5) of all SNe in the case of $n_i = 3\,\mathrm{cm}^{-3}$ and $\dot{N}_{\mathrm{SN,KS}}$ for run R-n_3 with random and run P-n_3 with peak driving. The temperature within the injection region, $T_{i,\,\mathrm{SN}}$, depends on the density. Typically, the temperature is $T_{i,\,\mathrm{SN}} > 2 \times 10^6$ K in the case of random driving. For peak driving, we find $T_{i,\,\mathrm{SN}} \gtrsim 10^6$ K, and for ~ 35 per cent of all explosions the temperature is below 10^6 K, leading to immediate strong cooling. For this reason, we explore a combined energy and momentum input model in Section 3.7.

3.6 Mixed driving

Peak and random driving represent two extreme cases of what we expect for the spatial distribution of SNe. To examine intermediate cases, we perform nine additional simulations with $n_i = 3\,\mathrm{cm}^{-3}$ and $\dot{N}_{\mathrm{SN,KS}}$ and different values of f_{peak}, the fraction of SNe going off in dense gas. Here, $f_{\mathrm{peak}} = 0$ per cent corresponds to random driving and $f_{\mathrm{peak}} = 100$ per cent corresponds to peak driving. In Fig. 9, we show the mass fractions (top left), pressures (top right), VFFs (bottom left), and 1D velocity dispersions (bottom right) as a function of f_{peak}.

Chemical composition. the ratio of atomic to molecular gas has a steep transition at $f_{\mathrm{peak}} \approx 50$ per cent. For $f_{\mathrm{peak}} > 50$ per cent the box is H I-dominated, which is typical for an ISM where the coldest component is removed by SN explosions within the dense gas. On the other hand, for $f_{\mathrm{peak}} < 50$ per cent, we find large amounts of

(Walch et al. 2012). However, one has to be cautious not to overestimate the effect of radiative cooling due to the finite numerical resolution of our models. Numerical overcooling acting at the interface between the cold shell and the hot interior of an SN bubble may reduce the amount of hot gas. More importantly, the density and, therefore, the mass within the SN injection region is high in the case of peak driving. Since we always inject an SN energy of 10^{51} erg per explosion, the effective temperature within the injection region can drop below 10^6 K in a dense environment. This is
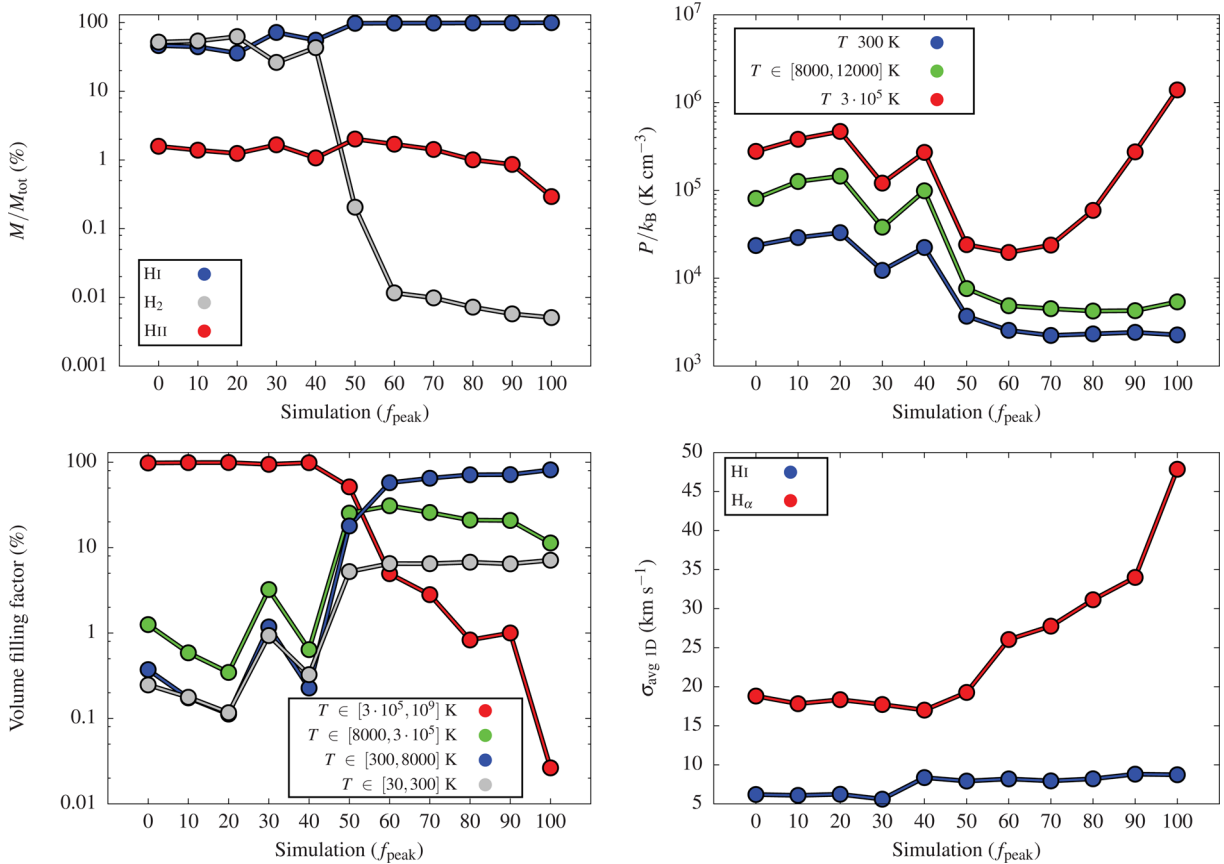

Figure 9. Average mass fractions (top left), pressures (top right), VFFs (bottom left), and 1D velocity dispersions (bottom right) as a function of f_{peak} for simulations using $n_i = 3\,\mathrm{cm}^{-3}$ and $\dot{N}_{\mathrm{SN,KS}}$.

molecular hydrogen since (i) a smaller f_{peak} disperses fewer dense clumps, and (ii) the larger number of uncorrelated SNe heat up the gas around the dense and cold medium and compress it (see Section 3.3).

Gas pressure. we find that all three phases are out of pressure equilibrium, although the pressures of the cold and warm phases decrease with increasing f_{peak} and these phases become close to isobaric for $f_{peak} > 50$ per cent. However, the hot gas pressure diverges for $f_{peak} > 50$ per cent as the SN remnants which contribute to this phase become younger and occupy smaller volumes. This has already been discussed for the case of pure peak driving (see Section 3.5).

VFF. a sharp transition at $f_{peak} \approx 50$ per cent can also be found for the VFFs of the different gas phases. For $f_{peak} \gtrsim 50$ per cent, the hot gas VFF drastically decreases while the VFFs of the warm and cold components are increasing. For small $f_{peak} < 50$ per cent, the number of random SN explosions is high enough to fill most of the box with hot gas and drive the box towards the thermal runaway regime.

H I and Hα velocity dispersion. with increasing peak fraction, the H I velocity dispersion increases from $\sim$5–6 km s^{-1} to $\sim$8–9 km s^{-1} at $f_{peak} \approx 40$ per cent. Also the Hα velocity dispersion increases for $f_{peak} \gtrsim 40$ per cent, from $\sim$18 to $\sim$48 km s^{-1} for $f_{peak} = 100$ per cent. For high f_{peak}, most of the Hα-emitting gas comes from young SN remnants (see Section 3.5).

3.6.1 Discussion: the transition between the peak and random driving regime.

Mixed driving, i.e. a combination of peak and random driving at different ratios, shows a relatively sharp transition in most ISM properties at a critical ratio of $f_{peak,crit} \approx 50$ per cent. It is likely that $f_{peak,crit}$ depends on the box density and SN rates. For instance, we expect $f_{peak,crit}$ to shift to higher values for higher average densities. It is also likely that $f_{peak,crit}$ shifts towards lower values if the periodic boundary conditions are relaxed and the box is allowed to 'breathe' (i.e. to adjust to local pressure equilibrium as gas is allowed to escape the box). In this case, the thermal runaway can also be delayed, leading to small $f_{peak,crit}$, or even avoided altogether. Thus, rather than being interested in extrapolating detailed physical conclusions, we are more keen on stressing once again that there are major differences in the properties of the ISM, which results from implementations of either peak or random driving.

3.7 Combined thermal energy and momentum injection

Due to our finite numerical resolution, the injection of thermal energy alone might lead to overcooling in dense regions (see Section 3.5.1 and Fig. 8). Therefore, we introduce an SN model, which allows us to switch from thermal energy to momentum input when the density in the vicinity of the SN is high and the Sedov–Taylor phase is unresolved (see Section 2.5.2). Using two simulations, we discuss how the combined model performs with respect to the thermal energy injection scheme. In particular, we redo run P-n_3, i.e. peak driving at $n_i = 3$ cm^{-3}, and run M50-n_3, i.e. mixed driving with $f_{peak} = 50$ per cent and $n_i = 3$ cm^{-3}. The corresponding new runs, which use the combined model, are called P-C-n_3 and M50-C-n_3.

The comparison between runs with and without momentum input suffers from uncertainties in the resolution of peak SNe with thermal energy injection. If unresolved, these SNe are prone to cool too quickly and the resulting momentum input could be underestimated (see Sections 2.5.2 and 3.8). On the other hand, the momentum injection method only takes into account the momentum-generating Sedov–Taylor phase and neglects the additional contribution from the pressure-driven snowplough phase (Section 2.5.2). Due to these intrinsic differences, a very detailed comparison is not possible at the moment.

In Fig. 10 (left-hand panel), we show that the Sedov–Taylor radius (equation 6) is unresolved, i.e. $R_{ST} < 4\Delta x$ as indicated by the green dashed line, for all SNe in run P-C-n_3 and for 63 per cent of the SNe in M50-C-n_3. In the latter case, the percentage of unresolved SNe being >50 per cent reflects the fact that most random SNe explode in a low-density environment, but not all of them. For the unresolved SNe, the injected momentum varies between 1 and 2×10^5 M$_\odot$ km s^{-1}, as shown in the right plot of Fig. 10. On a side note, if we instead require that the temperature within the injection region is higher than 10^6 K, we find that R_{ST} as given in equation (6) is somewhat conservative and could safely be increased by a factor of $\sim$1.6.

In Fig. 11, we compare the properties of the resulting ISM for runs with pure thermal energy injection and the new combined SN scheme. Here, the lines connect the models with the old and the new combined model.
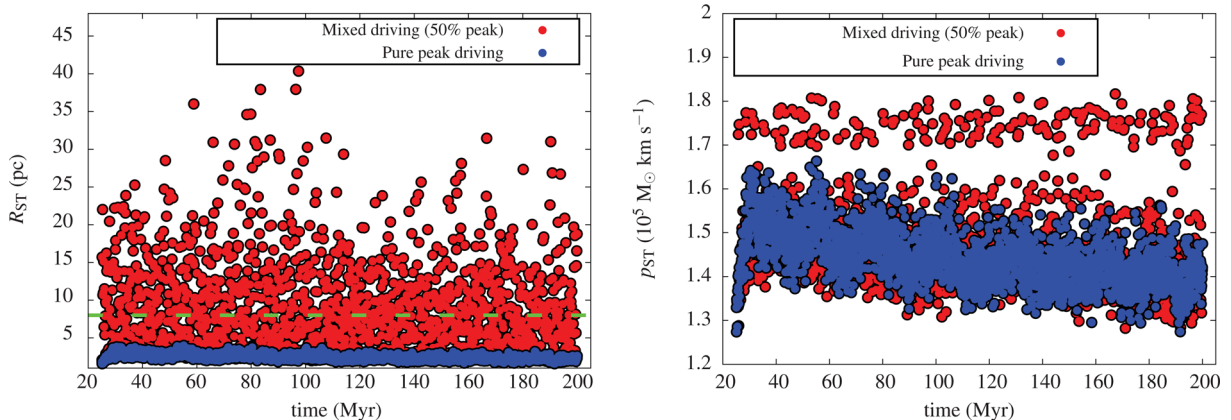

Figure 10. Radius at the end of the Sedov–Taylor phase (equation 6; left) and injected momentum (equation 7; right) for runs with pure peak driving (run P-C-n_3) and mixed driving with $f_{peak} = 50$ per cent (run M50-C-n_3). The dashed lines shows the resolution limit of $4\Delta x$, below which SNe are modelled via momentum input.
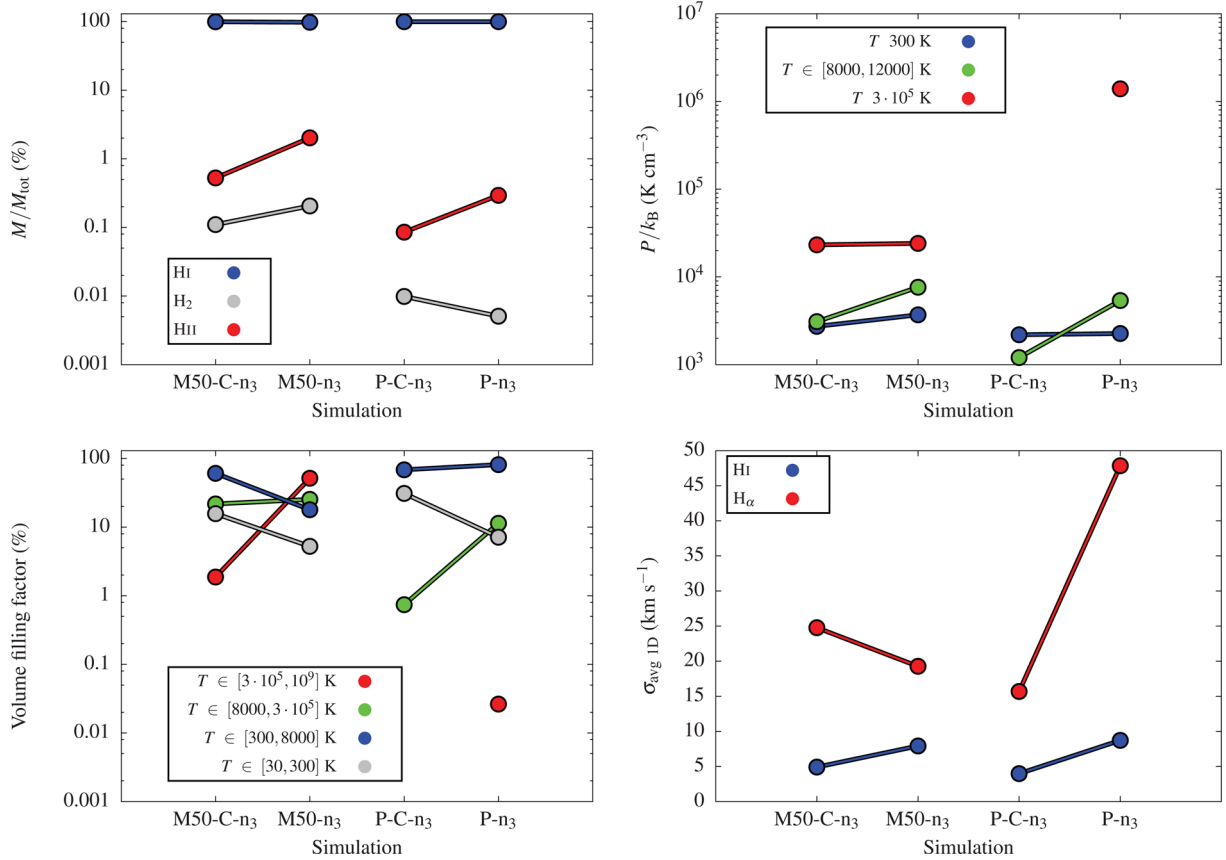
Figure 11. Average mass fractions (top left), pressures (top right),VFFs (bottom left), and 1D velocity dispersions (bottom right) for the momentum input simulations with $n_i = 3\,\mathrm{cm}^{-3}$ and $\dot{N}_{\mathrm{SN,KS}}$. The points are mixed driving with 50 per cent peak with combined thermal and momentum injection (M50-C-n_3); mixed driving with 50 per cent peak with thermal energy injection (M50-n_3); pure peak driving with combined injection (P-C-n_3); pure peak driving with thermal energy injection (P-n_3). The values are the average over the last 5 Myr of each simulation. The different lines connect simulations with same n_i, SN rates, and driving modes, but different injection methods.

Chemical composition. for both cases (peak and mixed driving), the two SN injection schemes give comparable mass fractions in all species. There are small differences, but these are well within the statistical fluctuations in the time evolution of each component (see the appendix for a discussion on the fluctuations).

Gas pressure. the main difference between the thermal energy injection and the combined SN injection scheme is that there is no hot gas present in the case of the combined model, if all the SNe are using the momentum input scheme. This is the case for run P-C-n_3 (see also Fig. 10) and therefore we cannot compare the pressures of the hot phase between the two approaches in the case of peak driving. If there is a random component (run M50-n_3), then the pressures of the hot phase are the same for thermal energy injection and combined model. The reason is that, in the case of thermal energy injection, SNe which explode in dense gas cool on short time-scales and do not contribute to the hot gas phase.

Furthermore, both mixed and peak driving show a slightly reduced pressure of the warm phase when the combined scheme is applied. For the mixed driving case (run M50-n_3), this brings the warm and the cold phase into pressure equilibrium. For the peak driving case (run P-C-n_3), the pressure of the warm phase appears to be smaller than the pressure of the cold phase. This is an artefact. Since the young SN bubbles themselves contribute significantly to the warm phase (because we set the temperature within the injection region to 10^4 K when momentum is injected), the warm phase is not

formed self-consistently in this simulation. However, the thermal energy injected in this way is between 1 and 9 per cent E_{SN}, with the majority of SNe lying in the range 1–5 per cent, in very good agreement with Kim & Ostriker (2014), Martizzi et al. (2014), and Walch & Naab (2014).

VFF. the VFFs of the cold gas increase when using the momentum input scheme, which is more efficient in dispersing dense gas than the thermal injection method. As described above, the hot phase is missing or negligible when modelling SNe with momentum injection.

H I and Hα velocity dispersion. the derived one-dimensional H I velocity dispersion is slightly lower for the combined model. The Hα emission is sensitive to the actual physical state of the warm component. Setting an upper temperature value of 10^4 K within the SN remnants strongly influences the derived Hα velocity dispersion. We do not recommend to trust the Hα velocity dispersion if the thermal state of the gas within the injection region has not been derived in a self-consistent way.

3.8 Higher resolution

As an alternative one may avoid having $T_{i,\,\mathrm{SN}} < 10^6$ K in the SN injection region by going to a higher numerical resolution. We run two additional simulations with resolution $\Delta x = 1$ pc with pure peak and random driving (with pure thermal injection) for our fiducial
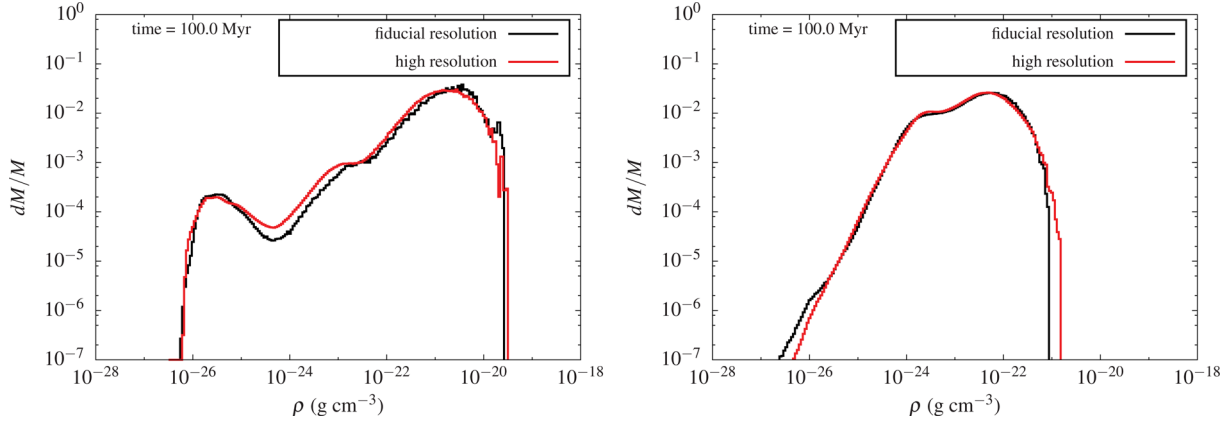
Figure 12. Mass-weighted density PDFs for random (left-hand column, runs R-n_3 and R-HR-n_3) and peak driving (right-hand column, runs P-n_3 and P-HR-n_3) for simulations with $\Delta x = 2$ pc (fiducial resolution) or 1 pc (higher resolution), and our fiducial parameters $n_i = 3$ cm^{-3} and $\dot{N}_{\mathrm{SN,KS}}$.

setup ($n_i = 3$ cm^{-3} and $\dot{N}_{\mathrm{SN,KS}}$). For peak driving, this increase of a factor of 2 in resolution shifts the fraction of SNe having an estimated $T_{i,\mathrm{SN}} > 10^6$ K from 65 to 96 per cent, while for random driving this value is close to unity in both cases. As shown in Fig. A2, simulations with different resolutions do not display any substantial discrepancy in their temporal evolution.

In Fig. 12, we compare the mass-weighted density PDFs for the fiducial and high-resolution simulations for random (left-hand panel) and peak driving (right-hand panel). We plot the mass-weighted PDF as this emphasises differences in the high-density regime, which is most critical. The density PDFs also show good convergence between fiducial and higher resolution, with an increase in density of rather less than a factor of 2.

Kim & Ostriker (2014) show that the conditions $R_{\mathrm{ST}} > 3\,\Delta x$ and $R_{\mathrm{ST}} > 3\,R_{\mathrm{inj}}$ should be satisfied in order to recover a final momentum close to the values retrieved from their high-resolution, sub-pc simulations. Combining these criteria and having assumed $R_{\mathrm{inj}} \geq 4\,\Delta x$ (equation 3), their requirements can be translated into $R_{\mathrm{ST}} > 12\,\Delta x$. This slightly differs from our criterion, where $R_{\mathrm{ST}} \geq R_{\mathrm{inj}} > 3\,\Delta x$. From equation (6) (but see also Section 3.7) $R_{\mathrm{ST}} \approx 30.6\,n^{-0.4}$ pc. Therefore, one can show that the critical density of the injection region (ambient medium) below which an SN is considered to be resolved is $n_{\mathrm{crit}} \approx 2$ cm^{-3} from the Kim & Ostriker (2014) criteria and $n_{\mathrm{crit}} \approx 59$ cm^{-3} from ours at our fiducial resolution of 2 pc. For $\Delta x = 1$ pc, $n_{\mathrm{crit}} \approx 10$ cm^{-3} from Kim & Ostriker (2014) and $n_{\mathrm{crit}} \approx 330$ cm^{-3} for us. For an initial density of 3 cm^{-3}, the highest densities reached are $n \sim 100$–500 cm^{-3} (see Fig. 12, right-hand panel) and, hence, only a fraction of SNe in the high-resolution run can be considered to be resolved. At fiducial resolution both ours and Kim & Ostriker (2014) conditions reveal that all of the SNe are not resolved (see also the left-hand panel of Fig. 10). Therefore, simulations with peak driving and thermal injection with initial density $n_i \geq 3$ cm^{-3} suffer from an underestimate of the momentum input by SNe and hence should be considered representative of a lower limit of the impact of peak SNe.

4 CONCLUSIONS

Summary. in this work, we perform 3D hydrodynamic simulations to study the SN-driven ISM in periodic volumes of size $(256\,\mathrm{pc})^3$. We include radiative cooling and diffuse heating, shielding from dust, and molecular gas (self-)shielding, as well as a chemical net-

work to follow H I, H II, H$_2$, CO, and C II. We study media with different mean gas densities, $n_i = 0.5, 1, 3, 10,$ and 30 cm^{-3}, which, integrated over the box side, correspond to surface densities of $\Sigma_{\mathrm{gas}} \approx 4, 8, 24, 81,$ and 243 M$_\odot$pc^{-2}. After an initial phase of turbulent stirring at rms velocity of 10 km s^{-1} for one crossing time (25 Myr), we switch to SN driving and follow the simulations for more than three additional crossing times.

The SN rates are constant for each simulation, but change with the mean box density according to the KS relation. We additionally perform models with a factor of 2 higher and lower SN rates. We explore the impact of the placement of the SNe relative to the dense gas. We distinguish between random positions (random driving), positioning on local density peaks (peak driving), and a mixture of the two (mixed driving). The different SN placements should reflect that SNe could explode (i) mostly in their birthplaces, where they might be deeply embedded (peak driving); (ii) preferentially in low-density environments (random driving). Random driving provides a simple way to introduce SNe in evolved, low-density environments without including all the necessary extra physics (wind and ionization feedback from massive stars; clustering of massive stars; runaway stars) acting in between the point of star formation and the SN explosion. For mixed driving, we perform a set of simulations where we explore different ratios of peak to random driving using the fiducial setup ($n_i = 3$ cm^{-3} and $\dot{N}_{\mathrm{SN,KS}}$).

Random driving at different supernova rates. in the case of random driving, most of the mass is in cold, dense atomic and molecular hydrogen, whereas most of the volume is filled with hot, rarefied gas. The ISM is out of pressure equilibrium in all simulations apart from two cases with lowest density and lowest SN rate. The synthetically observed 1D velocity dispersions are ~5–7 km s^{-1} in H I and ~17–25 km s^{-1} in Hα. Increasing the SN rate by a factor of 2 leads to an increase in the mean gas pressure of the different phases (cold, warm, hot medium), a small increase in the velocity dispersion (~ few km s^{-1}), and higher H I mass fractions, while the H$_2$ mass fractions decrease. However, the volume is always completely filled with hot gas, unless we consider low densities ($n_i \leq 1$ cm^{-3}) and SN rates of $\dot{N}_{\mathrm{SN}} \lesssim 2$ Myr^{-1}. We attribute this behaviour to a thermal runaway process (see Section 3.3), which occurs at high pressures, where only the cold branch of the equilibrium cooling curve can be reached, and no two-phase medium can form. In our case, though, the pressures are artificially determined. The boxes are not allowed to reach

hydrostatic equilibrium to a larger galactic potential, so the SNe continuously feed energy into the high-pressure, hot medium. Thus, they can push almost all of the gas mass into small, molecular clumps that quickly form molecular hydrogen.

Peak and mixed driving. for peak instead of random driving, the ISM has a completely different structure. It is dominated by a filamentary distribution of warm gas (mostly H I), with little to no hot gas present. SNe that explode in dense gas also disperse the cold medium, and therefore, the mass fraction of molecular hydrogen is small. The absence of hot gas (volume filling fraction VFF $\ll 50$ per cent) is due to the low heating efficiency and strong cooling of the SNe, which interact with dense gas. However, due to our limited resolution, we note that the impact of peak SNe is probably underestimated in high-density regions (for $n > 1$–$60\,\mathrm{cm}^{-3}$ with fiducial and $n > 10$–$300\,\mathrm{cm}^{-3}$ with high resolution). In these cases, one should anyway expand the model to include other important physical conditions and processes, such as stellar clustering, stellar winds, and ionizing radiation, and non-constant SN rate are critical ingredients, that shape the ISM and have to be taken into account.

For the setup with $n_i = 3\,\mathrm{cm}^{-3}$ and $\dot{N}_{\mathrm{SN,KS}}$, we vary the fraction of peak driving to random driving to explore the effect of a mixed SN placement at different fractions f_{peak}. A relatively sharp transition between the two regimes (peak and random) occurs when ~ 50 per cent of the SN are located within density peaks. As f_{peak} increases, the mass fraction in H_2 drops, and the VFF of the warm and cold gas decreases. Interestingly, we find that the pressure of the hot phase as well as the velocity dispersion in Hα increase with increasing peak fraction (H$\alpha \sim 50\,\mathrm{km\,s^{-1}}$ for 100 per cent peak driving). This behaviour can be attributed to the younger age of the SN remnants that contribute to these quantities.

Combined energy and momentum input. in low-density gas, the SNe are well resolved and we model them with thermal energy input. Explosions within high-density regions are eventually unresolved and would be subject to strong radiative (over)cooling. Therefore, we introduce a new model, which combines thermal energy input for resolved SNe and momentum input for unresolved SNe. The momentum input at the end of the Sedov–Taylor phase is calculated using the relations derived in Blondin et al. (1998). We put the model to work in two of the simulations (peak driving and mixed driving at $f_{\mathrm{peak}} = 50$ per cent). We find that the momentum input model fails to produce any hot gas because the shock speeds are too small to heat the medium to more than 10^4 K. Otherwise, the combined model gives similar results to the thermal energy injection model and is therefore a viable alternative to model SN in partly unresolved environments – with the limitation that the temperature structure of the gas is no longer self-consistent.

Clumpy H_2 in gas-rich discs. when thermal runaway sets in, hot gas at high pressure pushes the gas into small and dense clouds, leading to a fast and efficient conversion from H I to H_2. Warm gas directly cools towards the cold branch of the equilibrium curve and, similar to the case of a high far-UV interstellar radiation field, a bistable equilibrium between the cold and warm phases does not exist anymore. We speculate that the molecular-dominated, very clumpy structure of the ISM in simulations with a high gas surface density $\Sigma_{\mathrm{gas}} \gtrsim 100\,\mathrm{M}_\odot\,\mathrm{pc}^{-2}$ could be a reasonable representation of systems with high gas surface densities and very high mid-plane pressures like ULIRGs (Downes & Solomon 1998, but see also Rosolowsky & Blitz 2005) or normal star forming galaxies at high redshift (Genzel et al. 2010) that have high gas fractions and SFRs (e.g. Tacconi et al. 2010, 2013). Their mid-plane pressures are three to four orders of magnitudes higher than for the Milky Way (Bowyer et al. 1995; Berghöfer et al. 1998; Jenkins & Tripp 2011)

and plausibly reach values of $P/k_B \sim 10^{6-7}\,\mathrm{K\,cm^{-3}}$ for surface densities of 100 $\mathrm{M}_\odot\,\mathrm{pc}^{-2}$ and above (Swinbank et al. 2011), very similar to our models for $n_i = 10$ or $30\,\mathrm{cm}^{-3}$ with random driving. Such high mid-plane pressure forces all the gas on to the cold branch of the equilibrium curve, so that it reaches densities that allow quick conversion from atomic to molecular gas. Thus, in high pressure, gas-rich environments, the sizes and masses of the collapsing and H_2 forming structures could be regulated by SN feedback. Our simulations show that the mass budget of the ISM can be dominated by molecular gas while, at the same time, this molecular gas is still found in small dense clumps with low filling factor surrounded by hot rarefied gas, rather than being evenly distributed. However, this picture needs to be refined with simulations of stratified, high-surface density discs (similar to Shetty & Ostriker 2012) and a more self-consistent treatment of star formation to address the issue of self-regulation in gas-rich environments. On the other hand, for low $\Sigma_{\mathrm{gas}} \sim 5\,\mathrm{M}_\odot\,\mathrm{pc}^{-2}$, where the ISM has reasonable pressures and VFFs, we find too little molecular gas. Here, we are probably missing the aid of self-gravity.

Limitations of the model. for peak driving, the limited resolution employed raises concerns about the effectiveness of density peak SNe. Recent results from Kim & Ostriker (2014) suggest that our models with pure thermal injection should be considered to be lower limits on the impact of peak driving on the ISM. For random SNe, in particular for intermediate $\Sigma_{\mathrm{gas}} \sim 10$–$100\,\mathrm{M}_\odot\,\mathrm{pc}^{-2}$, the creation of high-pressure, high VFF, hot gas in the random driving case is overestimated due to our choice of periodic boundary conditions in all three dimensions. In a stratified disc, these high pressures would power a galactic fountain or outflow, lowering the ambient pressure in the mid-plane to the hydrostatic equilibrium value within a crossing time (few dozens of Myr) of a scaleheight for the hot gas. Other key physical ingredients, such as ionizing radiation, stellar winds, and stellar clustering, etc., could also play a crucial role in determining the state of the multiphase ISM. For these reasons, the employment of the simplified setup presented here does not allow us to draw any quantitative conclusions. However, this kind of study clearly shows the qualitative consequences of each model.

REFERENCES

Aggarwal K. M., 1983, MNRAS, 202, 15p
Anderson H., Ballance C. P., Badnell N. R., Summers H. P., 2000, J. of Phys. B: At. Mol. Phys., 33, 1255
Anderson H., Ballance C. P., Badnell N. R., Summers H. P., 2002, J. Phys. B: At. Mol. Phys., 35, 1613
Balsara D. S., Kim J., Mac Low M.-M., Mathews G. J., 2004, ApJ, 617, 339
Banerjee R., Vázquez-Semadeni E., Hennebelle P., Klessen R. S., 2009, MNRAS, 398, 1082
Berghöfer T. W., Bowyer S., Lieu R., Knude J., 1998, ApJ, 500, 838
Blaauw A., 1961, Bull. Astron. Inst. Neth., 15, 265
Blondin J. M., Wright E. B., Borkowski K. J., Reynolds S. P., 1998, ApJ, 500, 342
Bouchut F., Klingenberg C., Waagan K., 2007, Numer. Math., 108, 7
Bouchut F., Klingenberg C., Waagan K., 2010, Numer. Math., 115, 647
Bowyer S., Lieu R., Sidher S. D., Lampton M., Knude J., 1995, Nature, 375, 212
Brighenti F., D'Ercole A., 1994, MNRAS, 270, 65
Caldú-Primo A., Schruba A., Walter F., Leroy A., Sandstrom K., de Blok W. J. G., Ianjamasimanana R., Mogotsi K. M., 2013, AJ, 146, 150
Cioffi D. F., McKee C. F., Bertschinger E., 1988, ApJ, 334, 252
Clark P. C., Glover S. C. O., Klessen R. S., 2012, MNRAS, 420, 745
Cox D. P., Smith B. W., 1974, ApJ, 189, L105
Creasey P., Theuns T., Bower R. G., Lacey C. G., 2011, MNRAS, 415, 3706
Dale J. E., Ngoumou J., Ercolano B., Bonnell I. A., 2014, MNRAS, 442, 694
de Avillez M. A., Breitschwerdt D., 2004, A&A, 425, 899
de Avillez M. A., Breitschwerdt D., 2007, ApJ, 665, L35
Dib S., Bell E., Burkert A., 2006, ApJ, 638, 797
Dong R., Draine B. T., 2011, ApJ, 727, 35
Downes D., Solomon P. M., 1998, ApJ, 507, 615
Draine B. T., 1978, ApJS, 36, 595
Draine B. T., 2011, Physics of the Interstellar and Intergalactic Medium. Princeton Univ. Press, Princeton, NJ
Dubey A. et al., 2008, in Pogorelov N. V., Audit E., Zank G. P., eds, ASP Conf. Ser. Vol. 385, Numerical Modeling of Space Plasma Flows. Astron. Soc. Pac., San Francisco, p. 145
Dubey A. et al., 2013, Int. J. High Perform. Comput. Appl., 551, L105
Eldridge J. J., Langer N., Tout C. A., 2011, MNRAS, 414, 3501
Elmegreen B. G., Lada C. J., 1977, ApJ, 214, 725
Elmegreen B. G., Scalo J., 2004, ARA&A, 42, 211
Eswaran V., Pope S., 1988, Comput. Fluids, 16, 257
Ferrière K. M., 2001, Rev. Mod. Phys., 73, 1031
Fryxell B. et al., 2000, ApJS, 131, 273
Fujii M. S., Portegies Zwart S., 2011, Science, 334, 1380
Fukui Y. et al., 2003, PASJ, 55, L61
Gatto A., Fraternali F., Read J. I., Marinacci F., Lux H., Walch S., 2013, MNRAS, 433, 2749
Gent F. A., Shukurov A., Fletcher A., Sarson G. R., Mantere M. J., 2013, MNRAS, 432, 1396
Genzel R. et al., 2010, MNRAS, 407, 2091
Gies D. R., 1987, ApJS, 64, 545
Gies D. R., Bolton C. T., 1986, ApJS, 61, 419
Glover S. C. O., Clark P. C., 2012, MNRAS, 421, 116
Glover S. C. O., Mac Low M.-M., 2007a, ApJS, 169, 239
Glover S. C. O., Mac Low M.-M., 2007b, ApJ, 659, 1317
Glover S. C. O., Federrath C., Mac Low M.-M., Klessen R. S., 2010, MNRAS, 404, 2
Gnat O., Ferland G. J., 2012, ApJS, 199, 20
Goodman A. A., Barranco J. A., Wilner D. J., Heyer M. H., 1998, ApJ, 504, 223
Gritschneder M., Naab T., Walch S., Burkert A., Heitsch F., 2009, ApJ, 694, L26
Habing H. J., 1968, Bull. Astron. Inst. Neth., 19, 421
Heiles C., Troland T. H., 2003, ApJ, 586, 1067
Heitsch F., Slyz A. D., Devriendt J. E. G., Hartmann L. W., Burkert A., 2006, ApJ, 648, 1052
Heitsch F., Naab T., Walch S., 2011, MNRAS, 415, 271
Hennebelle P., Iffrig O., 2014, A&A, 570, A81
Hewitt J. W., Yusef-Zadeh F., 2009, ApJ, 694, L16
Hill A. S., Joung M. R., Mac Low M.-M., Benjamin R. A., Haffner L. M., Klingenberg C., Waagan K., 2012, ApJ, 750, 104
Hopkins P. F., Kereš D., Oñorbe J., Faucher-Giguère C.-A., Quataert E., Murray N., Bullock J. S., 2014, MNRAS, 445, 581
Iffrig O., Hennebelle P., 2014, preprint (arXiv:1410.7972)
Jenkins E. B., Tripp T. M., 2011, ApJ, 734, 65
Joung M. K. R., Mac Low M.-M., 2006, ApJ, 653, 1266
Joung M. R., Mac Low M.-M., Bryan G. L., 2009, ApJ, 704, 137
Kalberla P. M. W., Dedes L., 2008, A&A, 487, 951
Kalberla P. M. W., Kerp J., 2009, ARA&A, 47, 27
Keller B. W., Wadsley J., Benincasa S. M., Couchman H. M. P., 2014, MNRAS, 442, 3013
Kennicutt R. C., Jr, 1998, ApJ, 498, 541
Kim J., 2004, J. Korean Astron. Soc., 37, 237
Kim C.-G., Ostriker E. C., 2014, preprint (arXiv:1410.1537)
Kim C.-G., Kim W.-T., Ostriker E. C., 2011, ApJ, 743, 25
Kim C.-G., Ostriker E. C., Kim W.-T., 2013a, ApJ, 776, 1
Kim J.-h., Krumholz M. R., Wise J. H., Turk M. J., Goldbaum N. J., Abel T., 2013b, ApJ, 779, 8
Klessen R. S., Hennebelle P., 2010, A&A, 520, A17
Krause M., Fierlinger K., Diehl R., Burkert A., Voss R., Ziegler U., 2013, A&A, 550, A49
Kritsuk A. G., Norman M. L., 2002, ApJ, 569, L127
Lada C. J., Lada E. A., 2003, ARA&A, 41, 57
Larson R. B., 1981, MNRAS, 194, 809
McCray R., Kafatos M., 1987, ApJ, 317, 190
McKee C. F., Ostriker J. P., 1977, ApJ, 218, 148
Mac Low M.-M., Klessen R. S., 2004, Rev. Mod. Phys., 76, 125
Mac Low M.-M., McCray R., 1988, ApJ, 324, 776
Mac Low M.-M., Balsara D. S., Kim J., de Avillez M. A., 2005, ApJ, 626, 864
Martizzi D., Faucher-Giguère C.-A., Quataert E., 2014, preprint (arXiv:1409.4425)
Mestel L., Spitzer L., Jr, 1956, MNRAS, 116, 503
Micic M., Glover S. C. O., Banerjee R., Klessen R. S., 2013, MNRAS, 432, 626
Norman C. A., Ferrara A., 1996, ApJ, 467, 280
Ostriker E. C., McKee C. F., Leroy A. K., 2010, ApJ, 721, 975
Péquignot D., Tsamis Y. G., 2005, A&A, 430, 187
Perets H. B., Šubr L., 2012, ApJ, 751, 133
Petric A. O., Rupen M. P., 2007, AJ, 134, 1952
Pflamm-Altenburg J., Kroupa P., 2010, MNRAS, 404, 1564
Portegies Zwart S. F., 2000, ApJ, 544, 437
Raymond J. C., Cox D. P., Smith B. W., 1976, ApJ, 204, 290
Rogers H., Pittard J. M., 2013, MNRAS, 431, 1337
Rohlfs K., Wilson T. L., 1996, Tools of Radio Astronomy. Springer-Verlag, Berlin
Rosolowsky E., Blitz L., 2005, ApJ, 623, 826
Salpeter E. E., 1955, ApJ, 121, 161
Saury E., Miville-Deschênes M.-A., Hennebelle P., Audit E., Schmidt W., 2014, A&A, 567, A16
Scannapieco E., Gray W. J., Pan L., 2012, ApJ, 746, 57
Schmidt M., 1959, ApJ, 129, 243
Sellwood J. A., Balbus S. A., 1999, ApJ, 511, 660

Sembach K. R., Howk J. C., Ryans R. S. I., Keenan F. P., 2000, ApJ, 528, 310

Sharma P., Roy A., Nath B. B., Shchekinov Y., 2014, MNRAS, 443, 3463

Shetty R., Ostriker E. C., 2012, ApJ, 754, 2

Shull J. M., Saken J. M., 1995, ApJ, 444, 663

Simpson C. M., Bryan G. L., Hummels C., Ostriker J. P., 2014, preprint (arXiv:1410.3822)

Slyz A. D., Devriendt J. E. G., Bryan G., Silk J., 2005, MNRAS, 356, 737

Stinson G., Seth A., Katz N., Wadsley J., Governato F., Quinn T., 2006, MNRAS, 373, 1074

Stone R. C., 1991, AJ, 102, 333

Swinbank A. M. et al., 2011, ApJ, 742, 11

Tacconi L. J. et al., 2010, Nature, 463, 781

Tacconi L. J. et al., 2013, ApJ, 768, 74

Tamburro D., Rix H.-W., Leroy A. K., Mac Low M.-M., Walter F., Kennicutt R. C., Brinks E., de Blok W. J. G., 2009, AJ, 137, 4424

Tammann G. A., Loeffler W., Schroeder A., 1994, ApJS, 92, 487

Tenorio-Tagle G., Bodenheimer P., 1988, ARA&A, 26, 145

Tenorio-Tagle G., Bodenheimer P., Franco J., Rozyczka M., 1990, MNRAS, 244, 563

Tenorio-Tagle G., Rozyczka M., Franco J., Bodenheimer P., 1991, MNRAS, 251, 318

Thacker R. J., Couchman H. M. P., 2000, ApJ, 545, 728

Turk M. J., Smith B. D., Oishi J. S., Skory S., Skillman S. W., Abel T., Norman M. L., 2011, ApJS, 192, 9

Vázquez-Semadeni E., Gazol A., Scalo J., 2000, ApJ, 540, 271

Vázquez-Semadeni E., Ryu D., Passot T., González R. F., Gazol A., 2006, ApJ, 643, 245

Waagan K., 2009, J. Comput. Phys., 228, 8609

Wada K., Meurer G., Norman C. A., 2002, ApJ, 577, 197

Walch S. K., Naab T., 2014, preprint (arXiv:1410.0011)

Walch S., Wünsch R., Burkert A., Glover S., Whitworth A., 2011, ApJ, 733, 47

Walch S. K., Whitworth A. P., Bisbas T., Wünsch R., Hubber D., 2012, MNRAS, 427, 625

Walch S., Whitworth A. P., Bisbas T. G., Wünsch R., Hubber D. A., 2013, MNRAS, 435, 917

Walch S. K. et al., 2014, preprint (arXiv:1412.2749)

Wolfire M. G., Hollenbach D., McKee C. F., Tielens A. G. G. M., Bakes E. L. O., 1995, ApJ, 443, 152

APPENDIX A: TEMPORAL EVOLUTION VERSUS TIME AVERAGE

In this section, we show the differences between the analysed quantities averaged over the last 5 Myr of each simulation and their full temporal evolution. Generally, due to our choice of stopping the simulations once a chemodynamical equilibrium is reached, different runs have different final times. This already introduces uncertainty when comparing different simulations with quantities averaged over the last 5 Myr.

Fig. A1 shows the evolution of mass fractions, VFFs, pressures, and velocity dispersions for the fiducial setup with pure random (left-hand column) and pure peak driving (right-hand column). For random driving, the evolution of the quantities is smooth and the time average fairly portrays the global trend. On the other hand, for peak driving this is not true anymore. Highly time-varying H_2 mass fraction, σ_{H_α}, hot gas pressure, and VFF cause the time average to be not completely representative of the temporal trend. This behaviour is also important when comparing simulations with same driving mode, as shown in Fig. A2 for peak driving with fiducial (left-hand column) and high resolution (right-hand column). This effect, although not significant, should be taken into account when comparing simulations.
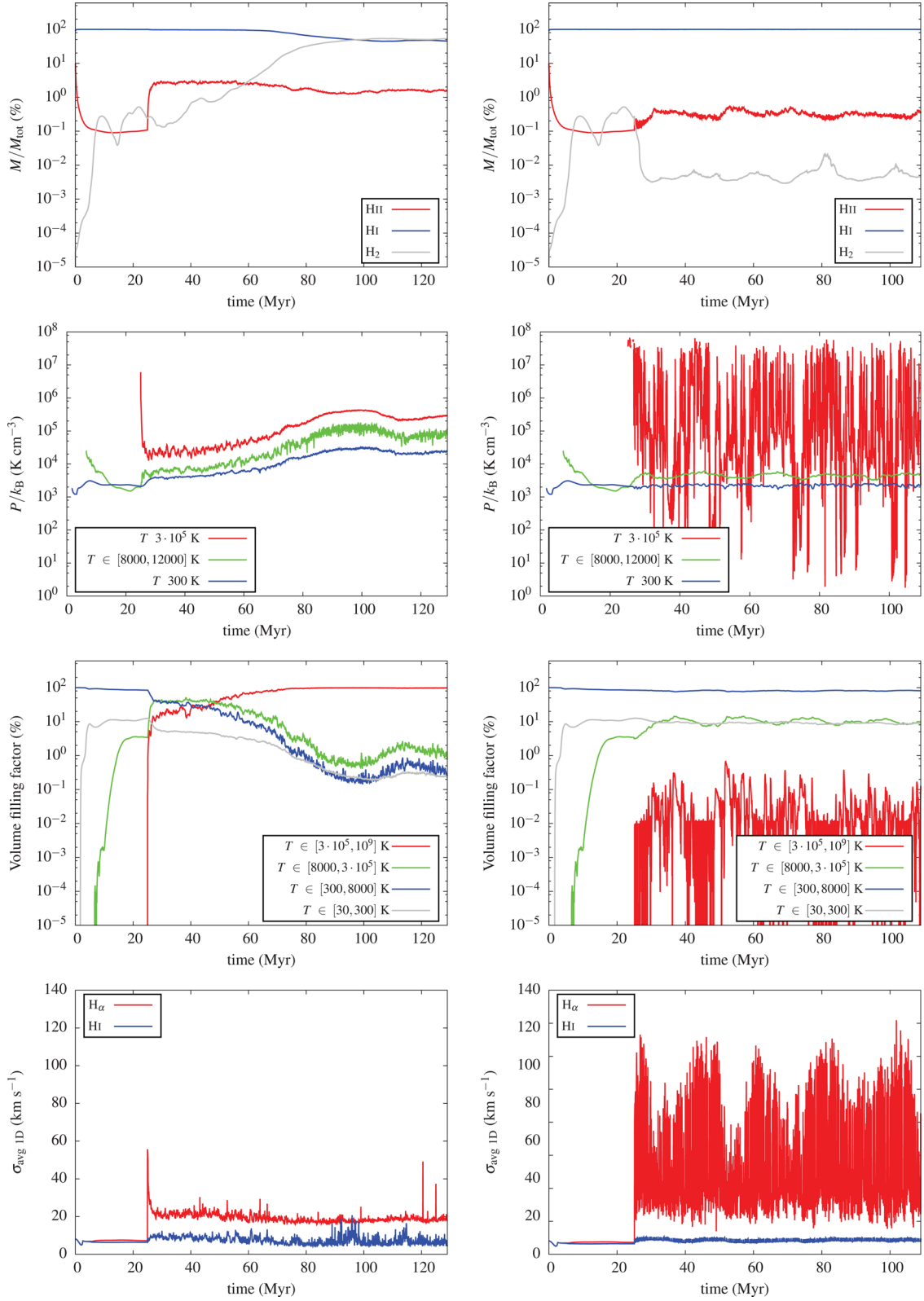
Figure A1. Evolution of mass fractions, pressures, VFFs, and velocity dispersions for $n_i = 3\,\mathrm{cm}^{-3}$ and $\dot{N}_{\mathrm{SN,KS}}$ with random (left-hand column) and peak driving (right-hand column).
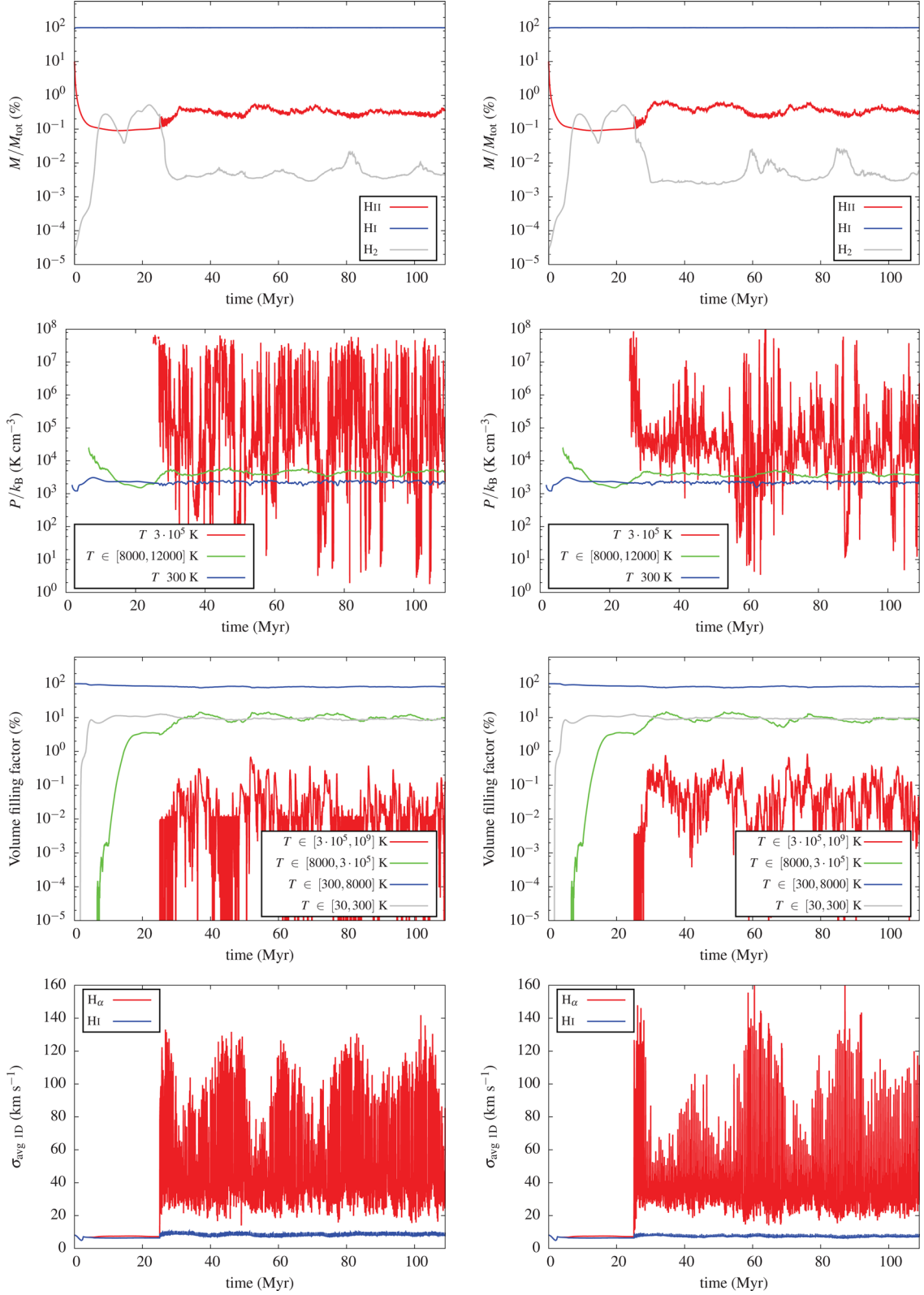
Figure A2. Evolution of mass fractions, pressures, VFFs, and velocity dispersions for $n_i = 3 \, \text{cm}^{-3}$ and $\dot{N}_{\text{SN,KS}}$ with peak driving for the fiducial resolution of $\Delta x = 2$ pc (left-hand column) and for higher resolution of $\Delta x = 1$ pc (right-hand column).

This paper has been typeset from a TeX/LaTeX file prepared by the author.